Laser-Induced Electron Diffraction in Chiral Molecules

Featured in Physics

Laser-Induced Electron Diffraction in Chiral Molecules

Debobrata Rajak,[1] Sandra Beauvarlet,[1] Omer Kneller,[2] Antoine Comby,[1] Raluca Cireasa,[3] Dominique Descamps,[1] Baptiste Fabre,[1] Jimena D. Gorfinkiel,[4] Julien Higuet,[1] Stéphane Petit,[1] Shaked Rozen,[2] Hartmut Ruf,[1] Nicolas Thiré,[1] Valérie Blanchet,[1] Nirit Dudovich,[2] Bernard Pons,[1] and Yann Mairesse[1]

[1]*Université de Bordeaux—CNRS—CEA, CELIA, UMR5107, Talence, France*
[2]*Weizmann Institute of Science, Rehovot 76100, Israel*
[3]*Institut des Sciences Moléculaires d'Orsay, CNRS, Université Paris-Saclay, UMR 8214, 91405 Orsay Cedex, France*
[4]*School of Physical Sciences, The Open University, Walton Hall, MK7 6AA Milton Keynes, United Kingdom*

(Received 17 July 2023; accepted 14 December 2023; published 12 February 2024)

Strong laser pulses enable probing molecules with their own electrons. The oscillating electric field tears electrons off a molecule, accelerates them, and drives them back toward their parent ion within a few femtoseconds. The electrons are then diffracted by the molecular potential, encoding its structure and dynamics with angstrom and attosecond resolutions. Using elliptically polarized laser pulses, we show that laser-induced electron diffraction is sensitive to the chirality of the target. The field selectively ionizes molecules of a given orientation and drives the electrons along different sets of trajectories, leading them to recollide from different directions. Depending on the handedness of the molecule, the electrons are preferentially diffracted forward or backward along the light propagation axis. This asymmetry, reaching several percent, can be reversed for electrons recolliding from two ends of the molecule. The chiral sensitivity of laser-induced electron diffraction opens a new path to resolve ultrafast chiral dynamics.

DOI: 10.1103/PhysRevX.14.011015

Subject Areas: Atomic and Molecular Physics, Chemical Physics

I. INTRODUCTION

Molecular chirality is a fundamental property of the microscopic world which rules the whole biosphere [1]. All living organisms are made of chiral building blocks (e.g., sugars or amino acids) that are not superimposable to their mirror image. One of these two images is systematically predominant in nature, and it is believed that this homochirality could be necessary for the emergence of life [1,2]. Despite its importance and impact, molecular chirality remains invisible to most experimental observations. This is due to the fact that a chiral structure can only be identified by using a chiral probe. Light-matter interaction was used as the first probe of molecular chirality by Biot in 1815, and has since then played a key role in chiral analysis. The two mirror images of a chiral molecule can be distinguished through their opposite rotations of the polarization axis of a linearly polarized electromagnetic field (optical activity) or through their different absorption of circularly polarized radiation (circular dichroism, CD) [3]. The continuous development of new chiroptical spectroscopies, such as vibrational CD [4], broadband electronic CD [5], or nonlinear optical spectroscopy [6], and their extension to the ultrafast time domain [7] have enabled significant breakthroughs in stereochemistry, providing a better understanding of the structure and dynamics of chiral compounds [8]. However, these techniques rely on electric-quadrupole or magnetic-dipole effects that produce relative signals in the 10^{-4} range, too weak to be detected in diluted samples. They are thus quasiexclusively applied in the condensed phase, where interactions between molecules or with the solvent can strongly affect the outcome of the measurements. A noticeable exception is the recent measurement of optical rotation in gases using an optical cavity [9]. Extending ultrafast chiroptical spectroscopy to the gas phase in order to study isolated compounds was thus necessary. Such extension would, for instance, enable us to elucidate the dynamical mechanisms of chiral recognition, through which two molecules identify themselves as left or right handed [10]. This challenge was overcome by the advent of new chiroptical techniques producing enantiosensitive signals of several percent within the electric-dipole approximation—the so-called "dipole

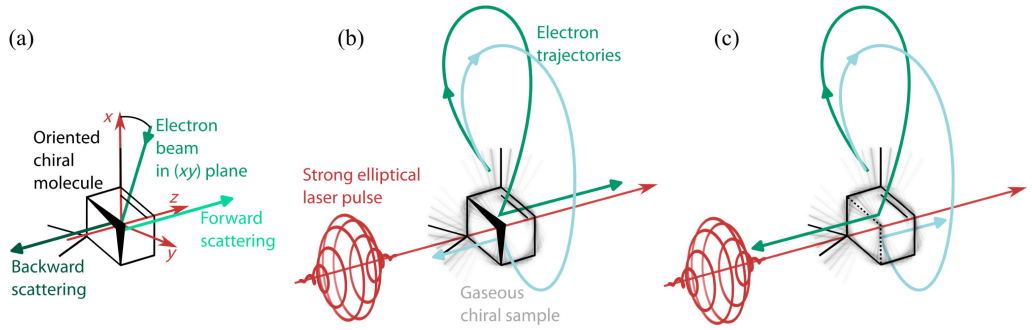

FIG. 1. Collisions between chiral molecules and electrons. (a) An electron beam impinging on an oriented chiral molecule is theoretically predicted to be preferentially scattered forward or backward from the incidence plane [38,39]. (b) Implementation of this idea by using an elliptically polarized strong laser field focused into a gaseous sample of chiral molecules. The laser field ionizes the molecules, selecting a preferential subset of molecular orientations. The released electrons are accelerated by the laser field following different trajectories in the polarization plane, and can be driven back to recollide with their parent ion from one side (green) or the other (blue) of the molecule. The electrons are preferentially scattered forward or backward on the light propagation axis, depending on the electron trajectory. This asymmetry reverses when switching from one enantiomer (b) to its mirror image (c).

revolution" in chiroptical spectroscopy [11,12]. Most of these techniques rely on the analysis of photoelectron angular distribution [13–19] and opened the route to ultrafast measurements of chiral dynamics in the gas phase, on the femtosecond [20–25] and attosecond [26] timescales. Chirosensitive signals emerging from electric-dipole interaction can also be revealed by microwave three-wave mixing [27–29], providing accurate information on chiral interactions which are of fundamental importance for analytical chemistry.

In parallel with the development of chiroptical spectroscopies, the question of using particle beams (electrons, positrons, neutrons) to probe molecular chirality has emerged. These particles can be spin polarized, and it was predicted that in that case they could interact differently with left-handed and right-handed molecules [30,31]. Such an asymmetric interaction was even proposed as a possible source of homochirality of life, in the Vester-Ulbricht hypothesis involving longitudinally polarized cosmic β radiation [2,32–34]. The first measurement of an electron dichroism effect was reported in 1985 [35], showing a surprisingly strong difference (∼0.5%) between the absorption of a 5 eV spin-polarized electron beam through gaseous samples of one or the other enantiomer of camphor. This effect was much larger than predicted and could not be reproduced [36]. Nevertheless, electron dichroisms could be observed when a heavy atom was attached to the probed chiral molecules, with asymmetries in the 10^{-4} range [36,37]. The weakness of the electron dichroism effects is intrinsic to the spin-based interactions ruling them. Drawing from the dipole revolution in chiroptical spectroscopy, one can wonder if it is possible to probe the molecular chirality with electron beams without relying on their spin. This idea was theoretically proposed two decades ago [38,39], and is described in Fig. 1(a). The target chiral molecule is oriented along an axis (x), and an electron beam is sent along a second direction in the (x, y) plane. The calculations predicted that in this geometry, the number of electrons scattered toward positive or negative z could differ by several 10%, and that this difference reversed with the handedness of the target molecule. However, the experimental demonstration of this effect has not been achieved so far due to the challenges in controlling the orientation of chiral molecules.

In this article, we solve this issue by using elliptically polarized strong laser fields to manipulate the collisions between electrons and oriented chiral molecules. We draw from laser-induced electron diffraction (LIED), which has recently emerged as a valuable alternative to conventional electron beam diffraction experiments [40–49]. LIED operates as follows: A strong laser field tunnel ionizes the molecule, accelerates the released electron, and drives it back to rescatter onto its parent ion. The differential cross section (DCS) resulting from this rescattering carries structural signatures of the ionic potential, enabling, for instance, retrieval of molecular structures with high accuracy and to follow ionic motion on the attosecond timescale (for a review, see, Refs. [50,51]). Up to now, LIED has been applied using linearly polarized driving pulses. Here we employ elliptically polarized strong laser fields, which opens the way to LIED imaging of chiral systems. As shown in Fig. 1(b), tunnel ionization selects a set of orientations within the randomly oriented sample every half cycle of the driving field [52,53]. The laser ellipticity, which influences the freed electron motion, is then employed to control the recollision angle of the electron with the selectively oriented molecules. Rescattering thus produces a large chirosensitive asymmetry in the final angular distribution of the scattered electrons, relative to the laser propagation direction, as depicted in Figs. 1(b) and 1(c). Importantly, the multiple quantum paths followed by the electron in the continuum enable probing the

molecule under different angles, which can even induce a sign change of the asymmetry when electrons recollide from opposite sides of a molecule. Our study fills the gap between light-matter and particle-collision probing of molecular chirality, as evidenced by the comparison of the electron beam diffraction scheme proposed by Busalla and coworkers [38,39] [Fig. 1(a)] and our chiral LIED setup [Figs. 1(b) and 1(c)]. Beyond the experimental demonstration presented below, chiral LIED is expected to resolve structural and dynamical features of chiral systems with angstrom spatial and subfemtosecond temporal resolutions, as in the case of conventional LIED [44,45,49,50,54].

II. ELECTRON DYNAMICS IN STRONG LASER FIELDS

We start by introducing the basic principles of strong-field light-matter interaction that will be used throughout the paper. The evolution of an atom or a molecule in a strong laser field can be described semiclassically as a sequential process [55–59]. First, around the maxima of the oscillating laser field, an electron can escape the binding potential by tunneling through the potential barrier lowered by the field. Second, this freed electron is accelerated by the laser electric field. The motion of the electron in the continuum is described by quantum paths which can be approximated by classical trajectories with a good accuracy [59]. Since the dynamics are driven by the strong laser field, the influence of the ionic potential on the electron trajectory can often be neglected (strong-field approximation [58]). Figures 2(b) and 2(d) show the result of a classical calculation solving Newton's equation of motion for a free electron driven by a linearly polarized cosine electric field [Fig. 2(a)]. Each electron trajectory is defined by the electron ionization time, its recollision time, as well as by its kinetic energy when it recollides.

If the electron is released slightly before the maximum of the laser field, it drifts away from the ionic core, gaining a maximum kinetic energy $2U_P$, where $U_P = I/4\omega_0^2$ is the ponderomotive potential determined by the intensity I and frequency ω_0 of the driving laser (atomic units are used throughout the paper). The periodicity of this process results in the well-known formation of above-threshold ionization peaks in the photoelectron spectra [60]. On the other hand, the electrons released slightly after the maximum of the field are subsequently driven back to the core as the laser field changes sign. Some of them can recombine radiatively and emit attosecond bursts of extreme ultraviolet (XUV) light, which is known as high-order harmonic generation (HHG) [61,62]. Alternatively, the electrons can experience a collision with the ion and be scattered off by the ionic potential [63]. Detecting the emitted photons or the rescattered electrons provides new ways of imaging molecular structures, through high-harmonic spectroscopy [64–66] or LIED [40–42,44,50].

Figure 2(b) shows a few selected electron trajectories. Some electrons recollide with their parent ion upon the first return (green trajectories). Other electrons keep on moving and recollide during their second or third return to the ionic core (blue and gray trajectories, respectively). As for the subsequent returns, our calculations (see Fig. 14) show that their contribution in elliptically polarized fields is insignificant. Remarkably, for all returns, two different electron trajectories lead to the same recolliding kinetic energy. For instance, the two green trajectories in Fig. 2(b) recollide with $2U_P$ energy, and the two blue trajectories recollide with U_P energy. These two families of electron trajectories, associated with two sets of quantum paths in the quantum mechanical description of the interaction [59], are labeled "short" and "long," Repeating the trajectory calculation for different ionization times enables us to extract the electron recollision energy for each family [Fig. 2(c)]. For the first returns, the maximum kinetic energy that the electrons can gain in the continuum is $3.17U_P$. The electrons recolliding at their second return were released within a much sharper time interval and their maximum kinetic energy at return is about twice smaller, reaching $1.54U_P$, while third return electrons recollide with a maximum energy of $2.41U_P$.

The electron-ion collisions considered here are elastic collisions, in which the kinetic energy of the electron is conserved but its direction can be reoriented as a result of the scattering. After the collision, the electron is further accelerated by the laser field. Conservation of momentum ensures that the final momentum of the electron is given by $\mathbf{p}_{\text{final}} = |\mathbf{p}_{\text{rec}}|\hat{\mathbf{e}} - \mathbf{A}(t_{\text{rec}})$, where $\hat{\mathbf{e}}$ is the direction of the scattered electron and $\mathbf{A}(t_{\text{rec}})$ is the laser vector potential at the time of recollision [50,67]. For each recolliding energy, the electrons end up on a sphere of radius $|\mathbf{p}_{\text{rec}}|$ centered on $-\mathbf{A}(t_{\text{rec}})$. The highest energy electrons recollide around the zeros of the laser field [Fig. 2(c)], i.e., when the vector potential is at its maximum value, $A_0 = 2\sqrt{U_P}$. Their recollisions thus produce spheres in momentum space, centered around $\pm A_0$, with radii $p_{\text{rec}}^{\text{first}} = \sqrt{2 \times 3.17U_P}$, $p_{\text{rec}}^{\text{second}} = \sqrt{2 \times 1.54U_P}$, and $p_{\text{rec}}^{\text{third}} = \sqrt{2 \times 2.41U_P}$ for first, second, and third returns, respectively. Cuts through these spheres are represented in Fig. 2(d), for electrons removed from the molecule around $t = 0$. The electrons released around the next maximum of the laser field ($t = T_0/2$) end up with the opposite longitudinal momentum p_x. In energy range, the direct photoelectrons extend to $2U_P$, the backscattered electrons from the first returns extend to about $10U_P$, those from second returns to $7U_P$, and those from third returns to $8.8U_P$.

The electron trajectories can be manipulated in two dimensions by controlling the ellipticity of the ionizing laser field. Figure 2(f) shows the short and long trajectories of electrons driven by a 1030 nm laser field at 2.5×10^{13} W cm^{-2}, polarized in the (x, y) plane with an ellipticity $\varepsilon = 0.3$ [shown in Fig. 2(e)]. The selected trajectories for the first return recollide with a $2U_P$

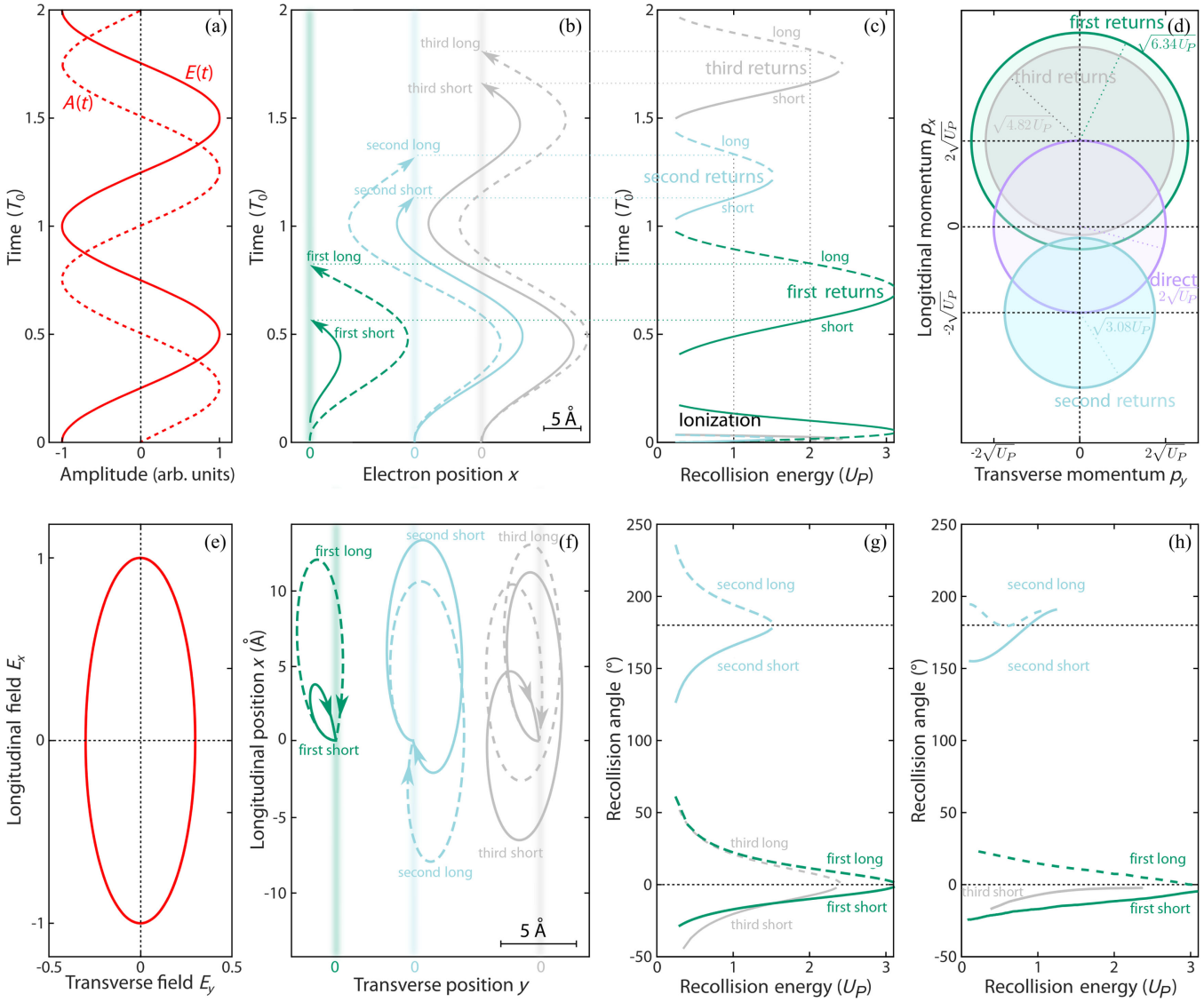

FIG. 2. Semiclassical electron dynamics in a strong laser field. (a) Temporal evolution of a linearly polarized electric field (continuous line) and vector potential (dashed line). (b) Example of electron trajectories in a 1030 nm linearly polarized laser field (period $T_0 = 3.44$ fs) at 2.5×10^{13} W cm^{-2}. The depicted green trajectories recollide with a kinetic energy of $2U_P$. The depicted blue trajectories recollide upon second return with a kinetic energy of U_P, and the depicted gray trajectories recollide upon third return with a kinetic energy of $2U_P$. (c) Ionization and recollision times as a function of the kinetic energy of the recolliding electron, for first (green), second (blue), and third (gray) return recollisions, and short (continuous) and long (dashed) trajectories. The maximum recollision energy is $3.17U_P$ for first returns, $1.54U_P$ for second returns, and $2.41U_P$ for third returns. (d) Final momentum of direct electrons (purple), ending up with a maximum energy of $p^2/2 = 2U_P$, and of indirect electrons after recollision upon first (green), second (blue), and third (gray) returns. (e) Elliptically polarized laser field, with $\varepsilon = 0.3$ ellipticity. (f) Example of classical electron trajectories in a 1030 nm laser field at 2.5×10^{13} W cm^{-2} with $\varepsilon = 0.3$. The first- (green) and third-return trajectories (gray) recollide with $2U_P$ energy. The second-return trajectories (blue) recollide with U_P energy. (g) Angle of the recolliding electron θ_{rec} as a function of recollision energy. (h) Same as (g) but using CTMC calculations including the influence of a hydrogenoid ionic potential.

energy (green). In order to recollide, the electrons must start with a transverse velocity that compensates for the lateral drift imposed by the laser ellipticity. The short trajectory escapes toward $y < 0$, travels about 5 Å away along the x direction, and recollides from this side. The long trajectory escapes toward the same direction but travels much farther away, about 15 Å, and recollides from $y > 0$. One can thus notice that the recollision angles θ_{rec} associated with the short and long trajectories, defined with respect to the $\hat{\mathbf{e}}_{\mathrm{x}}$ unit vector, have opposite signs [Fig. 2(g)]. This behavior was confirmed by trajectory-resolved high-harmonic polarimetry measurements [68].

Let us now turn our attention to the trajectories leading to recollision upon the second return. These electrons also start toward $y < 0$ but with a smaller transverse velocity compared to the first returns. Consequently, they are offset toward $y > 0$ when they come back to the $x = 0$ plane the first time, and miss the core. They keep on traveling toward $x < 0$ before reverting their motion and recolliding. The trajectories for the second return are all longer than for the first return. Short and long trajectories recollide with opposite angles with respect to the main axis of the laser polarization ellipse. Furthermore, the recollision angles are shifted by 180° with respect to the first returns. Lastly, the electrons recolliding upon third return show recollision angles within the same range as the first returns.

The different dynamics of the trajectories in the continuum not only affects the recollision angle, but also the sensitivity of the recollision probability to laser ellipticity [69,70]. This can be intuitively understood from the trajectories plotted in Fig. 2(f). Within the semiclassical description of the interaction, the electrons emerge from the tunnel with no longitudinal velocity, but with a Gaussian transverse velocity distribution centered around zero [71]. The width of this velocity distribution is dictated by the tunneling process. Figure 2(f) shows that the initial transverse velocity necessary to close a first- or third-return trajectory is larger than the one needed to close a second-return trajectory [69]. This classical picture has been quantitatively confirmed by measurements in rare gas atoms [70] as well as by 3D semiclassical calculations including the influence of the ionic potential on the electron trajectories [72]. These studies further demonstrated that the contribution from second returns dominates for ellipticities above $\varepsilon \sim 0.2$, consistently with the shape of the transverse velocity distribution of freed electrons.

The calculations presented in Figs. 2(a)–2(g) are performed within the strong-field approximation, which neglects the influence of the ionic potential on the electron trajectories. High-order harmonic polarimetry experiments have shown that this framework accurately describes the dynamics of first returns, but that the recollision angle of the low-energy long trajectories was decreased by a few degrees by the Coulomb focusing effect of the ionic potential [68]. The influence of Coulomb focusing was shown to be much stronger on second- and third-return trajectories, due to the attraction of the ionic potential as the electron passes near the ionic core. This increases the weight of multiple returns in recollision signals [73,74] and decreases the recollision angles of the electrons [75]. To quantify this effect, we performed classical trajectory Monte Carlo calculations (CTMC), simulating the classical electron dynamics under the combined action of the laser field and ionic potential. Figure 2(h) displays the recollision angles of the different electron trajectories. For first returns, the results are very similar to those obtained in Fig. 2(g), as already established in Ref. [68]. For second returns, the maximum kinetic energy of the recolliding electrons is slightly lowered and the recollision angles of the long trajectories are significantly distorted around their cutoff energy. For third returns, only the short trajectories are observed (see Appendix C), and their recollision angles are strongly diminished by the Coulomb focusing, e.g., from about 11° to 2° at $2U_P$ return energy.

The results of the simple calculations of Fig. 2 show that changing the laser ellipticity enables controlling the recollision angle of the electrons with their parent ion, and that different families of electron trajectories recollide from different directions. For first returns, the ionic potential hardly influences the electron motion. On the other hand, Coulomb focusing has a major influence on third-return electrons, bringing their recollision angles close to zero.

III. SYMMETRY BREAKING AND MOLECULAR ORIENTATION SELECTIVITY BY STRONG-FIELD IONIZATION

Manipulating the incidence angle of an electron beam colliding with a chiral sample is not sufficient to produce a chirosensitive signal. It is also necessary to control or select the orientation of the chiral molecules, as shown by Thompson [76] and illustrated in Fig. 1(a). Within the past two decades, important progress has been made to control the alignment and orientation of molecules in the gas phase using sophisticated schemes [77–79]. Such control is, however, not necessary to perform chiral laser-induced electron diffraction, because the strong-field ionization intrinsically enables us to select a set of molecular orientations from an ensemble of randomly oriented molecules. The anisotropy of tunnel ionization has been demonstrated in various molecular systems by measuring the ionization yields as a function of molecular alignment and orientation [52,53,78,80–83]. To evaluate this anisotropy in a chiral molecule, we employed the molecular orbital Ammosov-Delone-Krainov theory [84,85]. We neglect the effect of the permanent dipole, since it was shown that interaction of the outgoing electron with the dipole left behind cancels the influence of the Stark shift on the ionization yield [86]. We computed the tunnel-ionization rate from the highest occupied molecular orbital (HOMO) of (+)-fenchone molecules submitted to a half cycle of a linearly polarized laser field with intensity 2.5×10^{13} W cm^{-2} at 1030 nm. Fenchone ($C_{10}H_{16}O$) is a chiral bicyclic terpene with two asymmetric carbons. It exists as a single conformer because of its rigid structure, making it a good prototypical system for chiral studies such as the one presented below. Figure 3 shows the angular dependence of the ionization rate $W(\Omega_{\mathrm{mol}})$ as a function of Ω_{mol}, the molecular orientation with respect to the laboratory frame. Isodensity contours of the HOMO are also depicted in the figure. The ionization probability is strongly anisotropic, maximizing when the outer electron density points in the direction opposite to the linearly

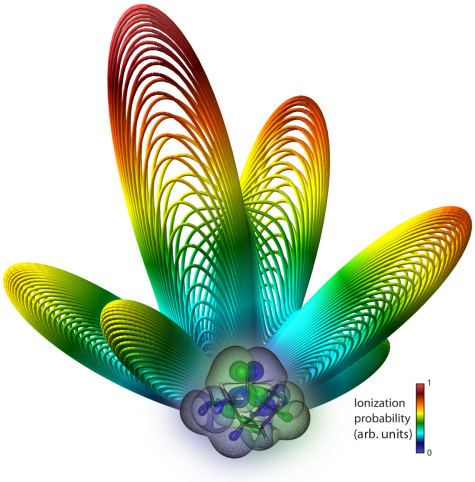

FIG. 3. Ionization probability of the highest occupied molecular orbital of a fixed-in-space fenchone molecule (depicted in blue and green isocontours) as a function of the orientation of a linearly polarized 1030 nm laser field at $I = 2.5 \times 10^{13}$ W cm^{-2}.

polarized field. This indicates that laser-induced tunnel ionization efficiently selects a set of molecules from the random distribution every half cycle of the driving field. In fenchone this orientation selectivity corresponds to the alignment of the C=O axis roughly parallel to the laser polarization. The selectivity can be confirmed by measuring the polarization state of the high-order harmonics generated in fenchone. In an isotropic medium submitted to a strong elliptical laser field, the polarization of the harmonics is expected to coincide with the electron recollision direction [87,88]. We show in Appendix A a strong deviation from this behavior, indicating an isotropy breaking of the medium by tunnel ionization.

While the orientation of the molecules is selected by the direction of the laser field at the time of ionization, the returning electron subsequently collides with the ionic core from a different direction. The strong elliptically polarized laser field thus defines a set of two noncollinear directions. However, this is insufficient to reveal the chirality of the target molecules within the dipole approximation. A difference of a few percent exists between the HHG signal produced by left- and right-handed elliptical fields in fenchone, but this effect results from the laser magnetic field [89]. In the following we focus on the geometrical requirements for observing a purely dipolar chiroptical signal [12] and show that this can be achieved by resolving the 3D momentum distribution of electrons after their elastic recollision with the oriented molecules selected by strong-field ionization.

IV. ELLIPTICAL DICHROISM FROM RECOLLIDING ELECTRONS

Inspired by Ref. [12], we start by summarizing the conditions to observe a chiral signal in an experiment. Mathematically, a simple chiral molecule can be described by a set of three mutually orthogonal unit vectors $\hat{\mathbf{e}}_1$, $\hat{\mathbf{e}}_2$, $\hat{\mathbf{e}}_3$, characterized by the pseudoscalar quantity $[\hat{\mathbf{e}}_1 \times \hat{\mathbf{e}}_2] \cdot \hat{\mathbf{e}}_3$. Pseudoscalar quantities are of fundamental importance in the theory of chiral phenomena [33]. They remain unchanged by any rotation of the vectors, but switch sign upon reflection. A pseudoscalar thus characterizes the handedness of a set of vectors. As stated in the Introduction, it takes a chiral probe to measure a chiral structure. The most common interpretation of this statement in the context of light-matter interaction is that circularly polarized light (CPL) is necessary to probe chiral molecules. The electric field of CPL indeed follows a helix in space and is thus chiral. This helix, which can be described by a pseudoscalar, is able to distinguish left-handed and right-handed molecules, giving rise to CD. Using the language introduced by Ayuso *et al.*, CPL is a chiral reagent [12]. However, the pitch of the helix, determined by the light wavelength, is generally much larger than the size of the probed molecules, leading to weak chiroptical interactions.

An alternative solution is to build a pseudoscalar by designing an experiment in which a set of three noncollinear vectors define the interaction [12]. Strong-field ionization in an elliptically polarized laser field defines two directions: (i) the direction of the laser field at the time of ionization, which is in good approximation the main axis of the laser polarization ellipse ($\hat{\mathbf{e}}_x$) and which determines the orientation of the molecules, and (ii) the recollision direction of the electron ($\hat{\mathbf{e}}_{rec}$), lying in the polarization plane but different from $\hat{\mathbf{e}}_x$. Resolving the outcome of the electron-molecule collision along the light propagation axis ($\hat{\mathbf{e}}_z$) enables building the pseudoscalar $[\hat{\mathbf{e}}_x \times \hat{\mathbf{e}}_{rec}] \cdot \hat{\mathbf{e}}_z$, producing chirosensitive signals.

This geometry is characteristic of the photoelectron circular dichroism (PECD) effect [13,14,90], in which chiral molecules are ionized by circularly polarized radiation. The chirality of the molecular potential induces an asymmetry in the scattering of the outgoing electrons, resulting in a forward-backward asymmetry of the photoelectron momentum distribution along the light propagation axis. The electric-dipole nature of PECD makes it very sensitive, with typical asymmetries in the 1%–10% range [17]. This effect is general in photoionization and exists in all regimes, single-photon [14], multiphoton [15,91], and tunnel ionization [18,92].

Figure 4(a) shows the 3D angle-resolved photoelectron distribution P obtained by photoionizing enantiopure fenchone molecules with circularly polarized 130 fs pulses at 1030 nm. The laser intensity is 2.5×10^{13} W cm^{-2}, which corresponds to a ponderomotive potential $U_P = 2.5$ eV. The Keldysh parameter $\gamma \approx 1.3$ indicates that the experiment takes place in the nonadiabatic tunneling regime. The 3D distribution was tomographically reconstructed [93] from a

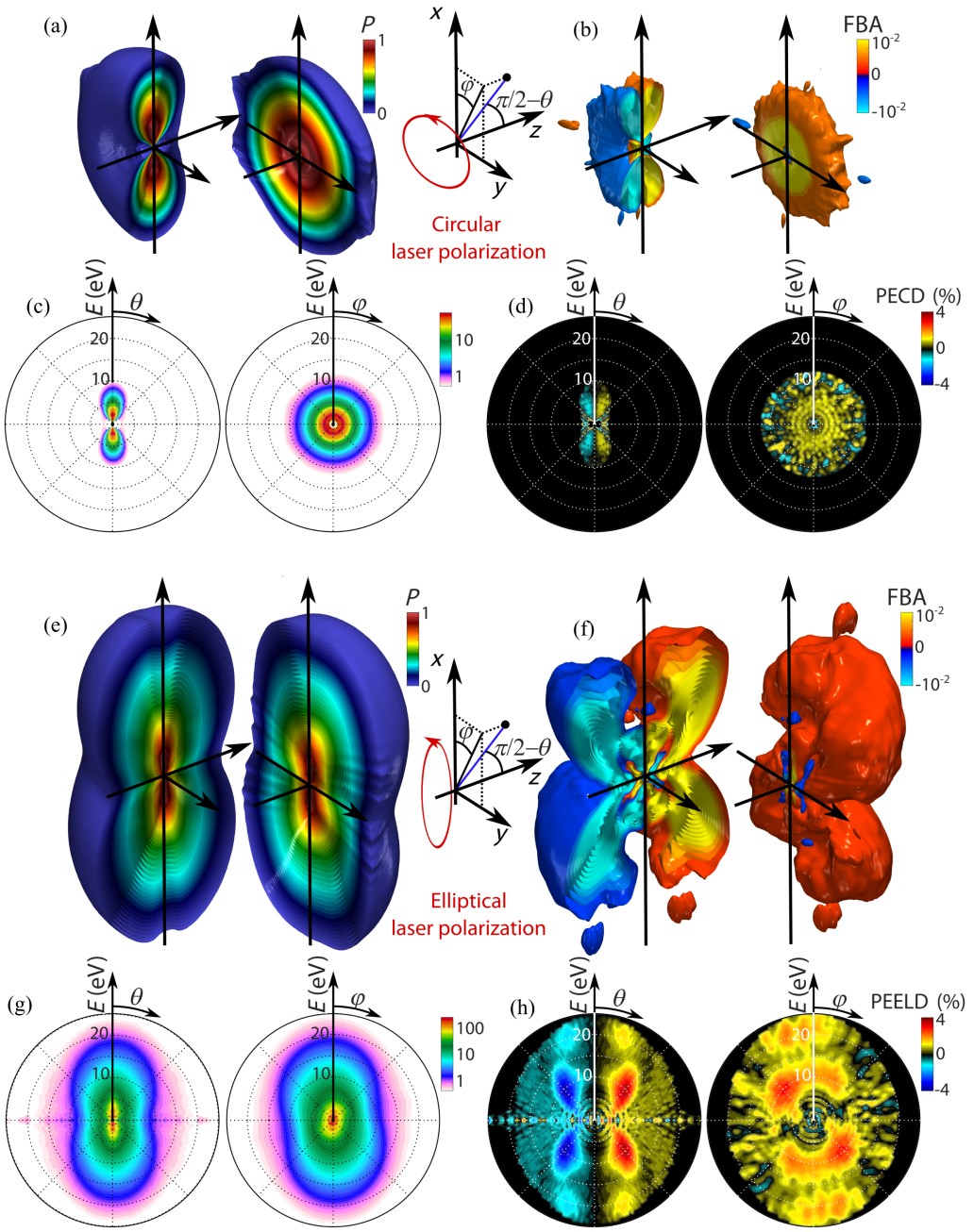

FIG. 4. Strong-field photoelectron dichroism in (+)-fenchone ionized by 2.5×10^{13} W cm^{-2} laser pulses at 1030 nm. (a) Energy-range 3D photoelectron angular distribution and (b) forward-backward asymmetric (FBA) part of the angular distribution, in circularly polarized light. (c) Angular dependence of the photoelectron spectrum and (d) of the PECD. The θ-resolved plots are integrated over $\varphi = [0, 2\pi]$. The φ-resolved plots are integrated over $\theta = [0, \pi]$, i.e., in the forward hemisphere. (e) Energy-range 3D photoelectron angular distribution and (f) FBA, in elliptically polarized light with $\varepsilon = 0.3$. (g) Angular dependence of the photoelectron spectrum and (h) of the PEELD.

set of projections recorded in a velocity map imaging spectrometer (see Appendix B). The distribution shows a cylindrical symmetry around the light propagation axis (z). For the analysis we introduce spherical coordinates drawn in the inset of Fig. 4. Integrating the data over φ provides the photoelectron spectrum as a function of the electron ejection angle θ with respect to the polarization plane [Fig. 4(c)]. The electron spectrum extends to approximately 7 eV, which corresponds to $2U_P$–$3U_P$. Indeed, the electrons driven by circularly polarized light do not recollide with their parent ion. The maximum kinetic energy that these direct electrons can gain from the field is $2U_P$, and the extra energy is gained through the interaction of the escaping electron with the ionic potential.

In principle the PECD can directly be evaluated by comparing the photoelectron distributions F and B in the forward and backward hemispheres, respectively. However, to minimize the influence of inhomogeneities in the detection, the PECD is alternatively obtained through a differential measurement between the distributions produced with left- and right-handed circular polarizations:

$$\mathrm{PECD} = 2\frac{F-B}{F+B} = 2\frac{P(\varepsilon=1)-P(\varepsilon=-1)}{P(\varepsilon=1)+P(\varepsilon=-1)}. \quad (1)$$

To improve the signal-to-noise ratio, we continuously varied the polarization state of the ionizing radiation by rotating a half wave plate in front of a fixed quarter wave plate, while recording the electron distribution on the fly. The resulting movie is Fourier analyzed to isolate the relevant periodic components from the noise and reconstruct the signal, in a similar manner as in a lock-in detection [19] (see Appendix B for details). We then extract the forward-backward asymmetric part (FBA) of the image by antisymmetrization [Fig. 4(b)]. The FBA shows an excess of electrons ejected forward, rather uniformly over the whole electron distribution. To quantify the strength of the chiroptical process, we calculate the PECD and represent its angular dependence in Fig. 4(d). The magnitude of the PECD is rather low, in the 1% range, which is typical of the strong-field regime [18]. When the laser ellipticity is reduced to $\varepsilon = 0.3$ [Figs. 4(e)–4(h)], we first observe an important extension of the photoelectron spectrum toward high energies, with electrons emitted beyond 20 eV. These high energies are reached by electrons that elastically collide with their parent ion, as in Fig. 2(d) [63,94]. The laser ellipticity clearly breaks the cylindrical symmetry of the electron distribution around the laser propagation axis $\hat{\mathbf{e}}_z$. The φ-resolved photoelectron spectrum shows that low-energy components (< 5 eV) maximize toward positive φ angles, whereas high-energy electrons maximize toward negative φ angles [Figs. 4(e) and 4(g)]. These different angular streakings in the elliptical laser fields are characteristic of direct and rescattered electrons [95], and are sensitive to the molecular potential [82]. The symmetry breaking leads us to redefine the chiroptical signal. In PECD, switching the helicity of the laser field is equivalent to switching the handedness of the molecule. This is not the case for elliptically polarized light [19]. We can nevertheless perform a differential measurement by using the fact that the photoelectron angular distribution P measured at ε in a given enantiomer [e.g., $(+)$] must be the mirror image relative to the (x,z) plane (noted as $*$) of the distribution measured in the opposite enantiomer [$(-)$] using the opposite ellipticity:

$$P^{(+/-)}(\varepsilon) = P^{*(-/+)}(-\varepsilon). \quad (2)$$

We thus extract the FBA through a doubly differential operation, using the signals acquired in a given enantiomer:

$$\mathrm{FBA}^{(+)}(\varepsilon) = \frac{1}{4}\{[F^{(+)}(\varepsilon) - B^{(+)}(\varepsilon)] - [F^{*(+)}(-\varepsilon) - B^{*(+)}(-\varepsilon)]\}. \quad (3)$$

The counterpart of PECD, the photoelectron elliptical dichroism (PEELD), is then defined as the normalized asymmetric signal:

$$\mathrm{PEELD}^{(+)}(\varepsilon) = 2\frac{\mathrm{FBA}^{(+)}(\varepsilon)}{F^{(+)}(\varepsilon) + B^{(+)}(\varepsilon)}. \quad (4)$$

In practice, we record this signal in both enantiomers, and average their opposite responses to remove any residual artifact in the detection. Raw data obtained in opposite enantiomers are presented in Fig. 13 of Appendix B.

The FBA recorded by photoionizing fenchone with elliptically polarized 1030 nm pulses ($\varepsilon = 0.3$) is depicted in Fig. 4(f). We observe a clear FBA beyond the energy range characterizing direct electrons, i.e., for energies larger than 5 eV. This observation demonstrates that the recollision of laser-driven electrons is sensitive to chirality. The φ-integrated PEELD shows butterfly wings maximizing around $\theta = 45°$ at 10 eV electron energy [Fig. 4(h)]. The PEELD reaches 4%, and is thus 4 times stronger than the PECD recorded with circularly polarized light. This is quite remarkable, since the third Stokes parameter of the ionizing radiation, which quantifies the excess of circularly polarized photons, is around 0.5. The asymmetry imprinted by the chiral potential upon backscattering is thus 8 times larger than the one imprinted on direct electrons. As the electron energy increases, the PEELD decreases but shows secondary maxima at high energy (>20 eV) for small ejection angles θ. The φ dependence of the PEELD shows that the asymmetry maximizes around $\varphi = -45°$ at 10 eV.

The sensitivity of the process to the structure of the ionized molecule can be evaluated by repeating the measurements in a different molecule. We chose α-pinene ($C_{10}H_{16}$), another bicyclic monoterpene structurally similar to fenchone and with a similar ionization potential, but which does not contain any oxygen atom. The 3D photoelectron angular distributions and the FBA measured with circularly polarized light [Figs. 5(a) and 5(d)] closely resemble the ones measured in fenchone. Importantly, however, the FBA measured with elliptical polarization is drastically different [Fig. 5(f)], showing sets of branches of alternating signs. The φ-integrated PEELD confirms this two-branch structure, with a main branch dominating at high ejection angles $\theta > 45°$ and

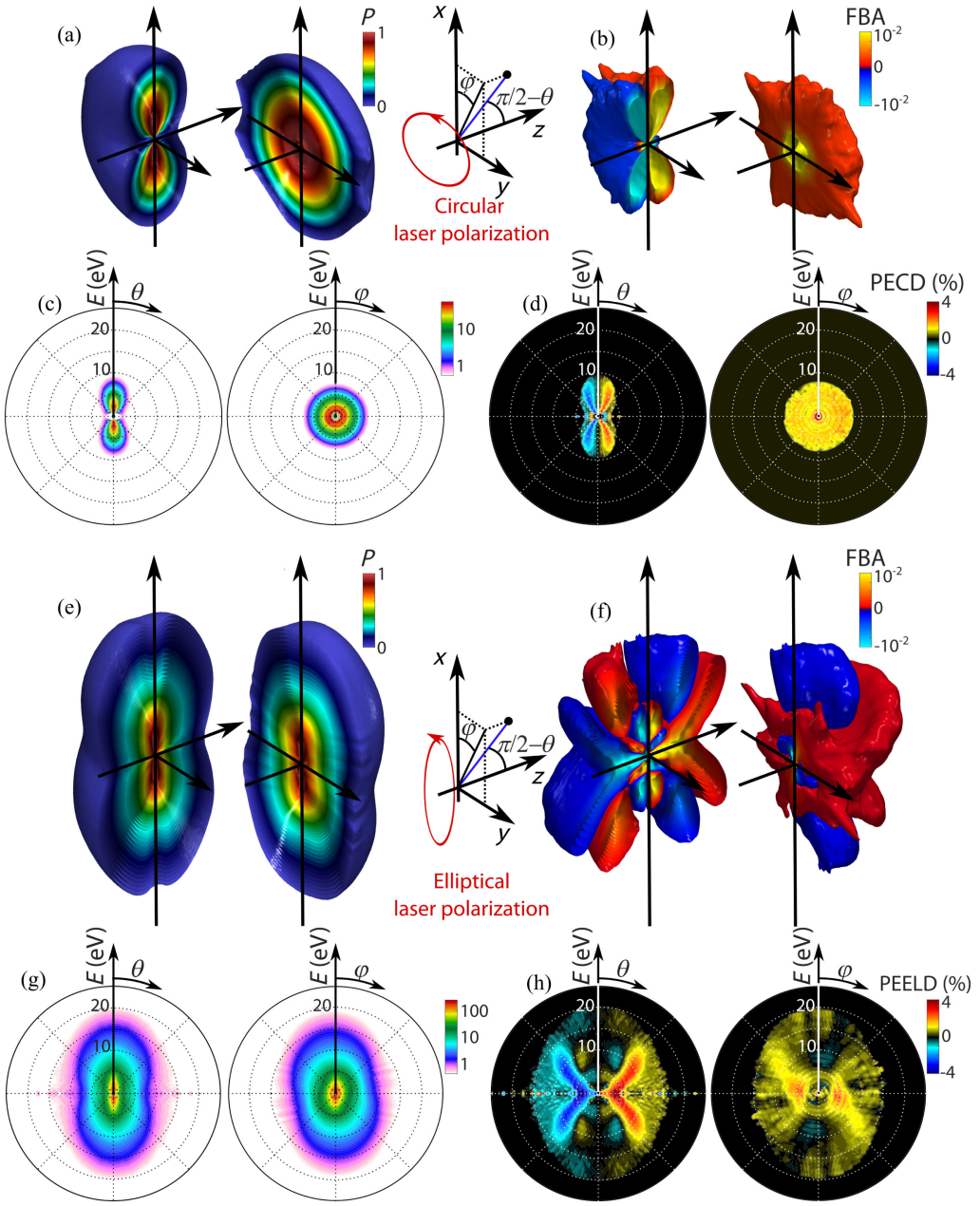

FIG. 5. Strong-field photoelectron dichroism in (+)-α-pinene ionized by 2.5×10^{13} W cm^{-2} laser pulses at 1030 nm. (a) Energy-range 3D photoelectron angular distribution and (b) forward-backward asymmetric part of the angular distribution, in circularly polarized light. (c) Angular dependence of the photoelectron spectrum and (d) of the PECD. The θ-resolved plots are integrated over $\varphi = [0, 2\pi]$. The φ-resolved plots are integrated over $\theta = [0, \pi]$, i.e., in the forward hemisphere. (e) Energy-range 3D photoelectron angular distribution and (f) forward-backward asymmetric part of the angular distribution, in elliptically polarized light with $\varepsilon = 0.3$. (g) Angular dependence of the photoelectron spectrum and (h) of the PEELD.

high energy, and a secondary branch maximizing around $\theta = \pm 30°$ and extending up to ~12 eV.

The emergence of these two branches with opposite FBAs is intriguing. In the following we show the connection between these branches and the first and second return electron trajectories introduced earlier in this article.

V. IDENTIFICATION OF ELECTRON TRAJECTORIES

In this section, we delve deeper into the recollision mechanism in order to assign the electron trajectories. The classical simulations shown in Fig. 2 indicate that up to six electron trajectories can lead to the same energy of the recolliding electron. The overlap of the different trajectories

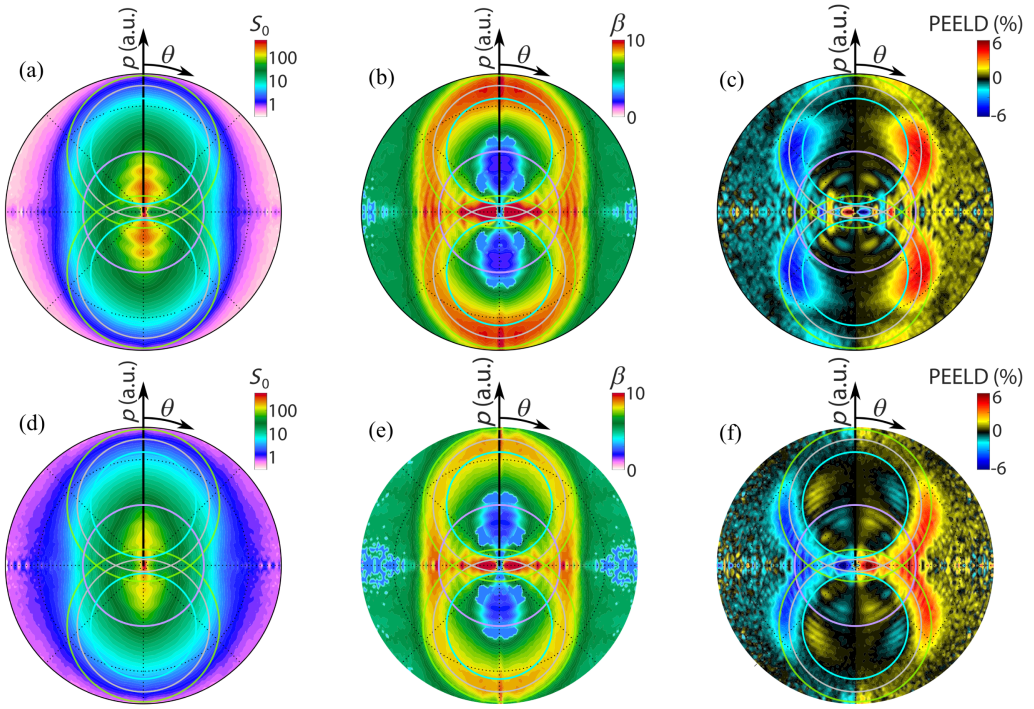

FIG. 6. Trajectory identification by ellipticity dependence measurements, averaged over photoelectrons detected in the $\varphi = [40–80]°$ range. (a) Photoelectron momentum distribution produced in (+)-fenchone by a 1030 nm laser pulse at 2.5×10^{13} W cm^{-2} with an ellipticity $\varepsilon = 0.3$. The circles depict the maximum momentum expected from direct electrons (purple) and from first return (green), second return (blue), and third return (gray) recollisions. (b) Decay rate β of the photoelectron signal as a function of ellipticity. (c) Forward-backward asymmetry of the electron signal. Panels (d)–(f) show the same measurements and analysis as (a)–(c), respectively, but for (+)-α-pinene.

produces complex structures in the electron momentum distribution, resulting from quantum interference effects [96]. In the case of HHG, macroscopic conditions can be found to select a single family of electron trajectories, the short first returns. However, in photoelectron spectroscopy the measured signal is the incoherent sum of the contributions from the different molecules and it is determined only by the ionization and recollision probabilities at the single-molecule level, without any macroscopic interference effect. The tunnel-ionization probability strongly depends on the width of the barrier, decaying exponentially as the laser field decreases. Figure 2(c) shows that the short trajectories of the first returns are initiated relatively late in the optical cycle, when the potential barrier is rather thick. Their contribution to the recollision signal is thus negligible, as demonstrated in Ref. [72]. This means that beyond the cutoff energy of the second and third returns (i.e., $> 8.8U_P$), the rescattered electrons originate preferentially from long trajectories of the first returns. This assumption is common to all laser-induced electron diffraction works [44,50]. What happens in the lower part of the electron momentum distribution, where multiple returns can contribute, remains to be determined.

We can assign the electron trajectories by following their response to the laser ellipticity. High-harmonic spectroscopy experiments have shown that the ellipticity dependence of the high-harmonic emission was dictated by the length of the electron trajectories in the continuum [97]. Following this idea, we measured the ellipticity dependence of the photoelectron angular distribution. Each component $\mathbf{p}$ of the 3D momentum distribution was fitted by $S(\mathbf{p}) = S_0 e^{-\beta(\mathbf{p})\varepsilon^2}$, where $\beta(\mathbf{p})$ is the decay rate of the photoelectron yield [98]. Figure 6 shows the result of this analysis for electrons ejected between $\varphi = 40°$ and $\varphi = 80°$, in fenchone [Fig. 6(b)] and α-pinene [Fig. 6(e)]. This electron ejection range selected for the analysis was based on maximizing the contribution of the outer branch in the PEELD signal from α-pinene.

The depicted photoelectron angular distributions and PEELDs, shown in Figs. 6(a) and 6(d) and in Figs. 6(c) and 6(f), respectively, correspond to $\varepsilon = 0.3$. The angle-resolved decay rate [Figs. 6(b) and 6(e)] shows three distinct areas, with very similar structures in fenchone and α-pinene. In the high-energy part of the distributions, between the cutoff of the first returns (green circles) and the cutoff of the second returns (blue circles), the photoelectron yield decays fast with ellipticity, with β in the 8–10 range. This is typical of the recollision process. Remarkably, the decay rate decreases sharply at the cutoff energy of the second returns (blue circles), falling to values around 5–7. This demonstrates that in this range, the contribution from second returns is dominant, consistently with Refs. [69,70,72]. Lastly, at low energy, below $2U_P$

(purple circle), and around the laser polarization plane ($\theta = 0$), the decay rate obtained from the Gaussian fits is very low. This is typical of direct electrons, which do not recollide. Turning our attention to the PEELD maps, we observe a striking correspondence between the areas identified by the decay rate and the different branches in the chiroptical response. In fenchone, the PEELD is strong in the area associated with first returns, and almost vanishes for second returns. In α-pinene, first and second returns show opposite PEELDs. We note that no trace of third returns can be identified in these maps. We attribute this lack of third-return signature to the reduction of the recollision angles by Coulomb focusing [as shown by the CTMC calculations in Fig. 2(h)], which prevents a significant chiroptical signal from these trajectories to emerge. We can now use the assigned areas of the distribution to perform trajectory-resolved chiral laser-induced electron diffraction.

VI. CHIRAL LASER-INDUCED ELECTRON DIFFRACTION

A. Measurements of differential cross sections

A schematic view of the trajectory-resolved laser-induced diffraction process is depicted in Fig. 7(a). Electrons are released by tunnel ionization around a maximum of the laser field. The anisotropy of the tunneling rate selects a subset of molecular orientations along a given direction $\hat{\mathbf{e}}_1$, as confirmed by the high-harmonic polarization measurements in Appendix A. The electrons recollide along another direction $\hat{\mathbf{e}}_2$, dictated by the trajectory. For first returns, the electrons recollide from the side of the molecule from which they tunneled out. The long trajectories dominate due to their larger ionization rate. For second returns, both short and long trajectories contribute to the recollision, and the electrons recollide from the opposite side of the molecule. We will disregard third-return trajectories because they do not show up in the analysis of the chiroptical signal, due to their reduced recollision angles imposed by Coulomb focusing.

Figures 7(b) and 7(d) show the angular distribution of rescattered electrons from first and second returns, obtained by cutting spheres through the measured 3D electron momentum distribution, measured in fenchone and α-pinene. The radii of the spheres correspond to the maximum kinetic energy of the recolliding electrons ($3.17U_P$ and $1.54U_P$, respectively), and the spheres are centered on the maxima of the vector potential. For first returns, we observe that more electrons are located at the bottom of the sphere. These electrons are only slightly deviated by the recollision. On the other hand, the electrons located on top of the sphere are those that have made a half-turn during the collision, and are much fewer. The evolution of the electron density over the sphere thus provides the DCS of the electron-ion scattering. A similar trend is visible on the lower spheres, associated with the second returns.

Figures 7(c) and 7(e) show the forward-backward asymmetric part of this DCS, which encodes the chiro-sensitive signal as predicted by Refs. [38,39,76]. For both molecules, first-return electrons are preferentially rescattered forward, as already seen in the PEELD distributions of Figs. 4 and 5. We note that the asymmetry shows a local minimum for intermediate scattering angles in fenchone. Turning our attention to the second returns, which recollide from the other side of the molecule, we find that they show

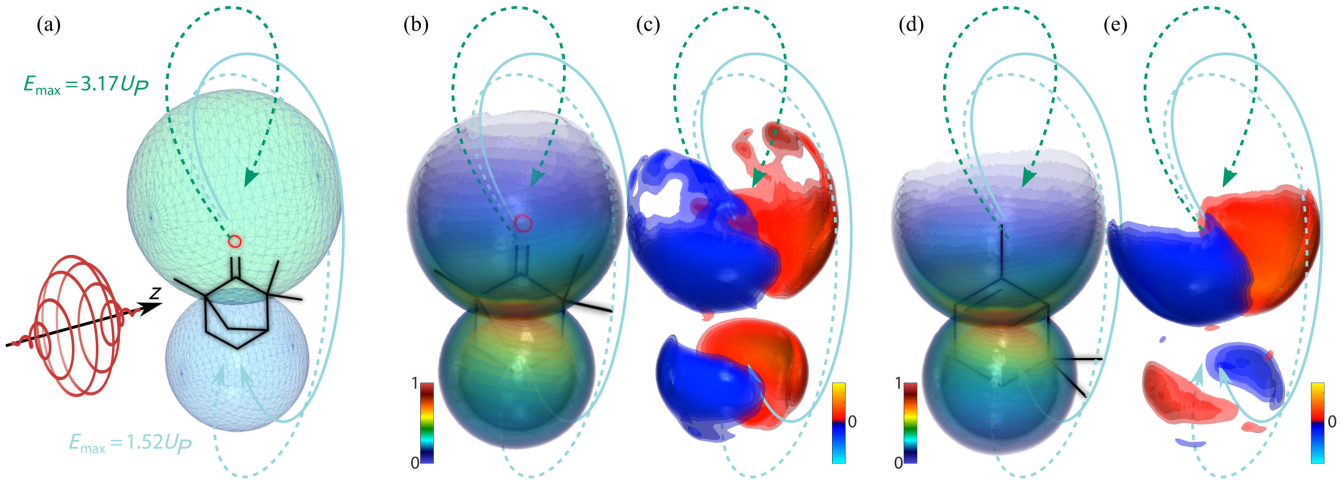

FIG. 7. Chiral laser-induced electron diffraction. (a) Schematic representation of the 3D momentum distribution upon recollision of first returns, long trajectories (green), and second return, short, and long trajectories (blue). The orientation of the molecule is selected by tunnel ionization and the recollision angles are dictated by the laser field and ellipticity. (b) Measured 3D momentum distribution produced by recollision on first (top) and second (bottom) returns in (+)-fenchone. (c) Forward-backward asymmetry of the momentum distribution, corresponding to the chiral laser-induced electron diffraction pattern. (d),(e) Same measurements in (+)-α-pinene, where the first and second return show opposite chiral responses.

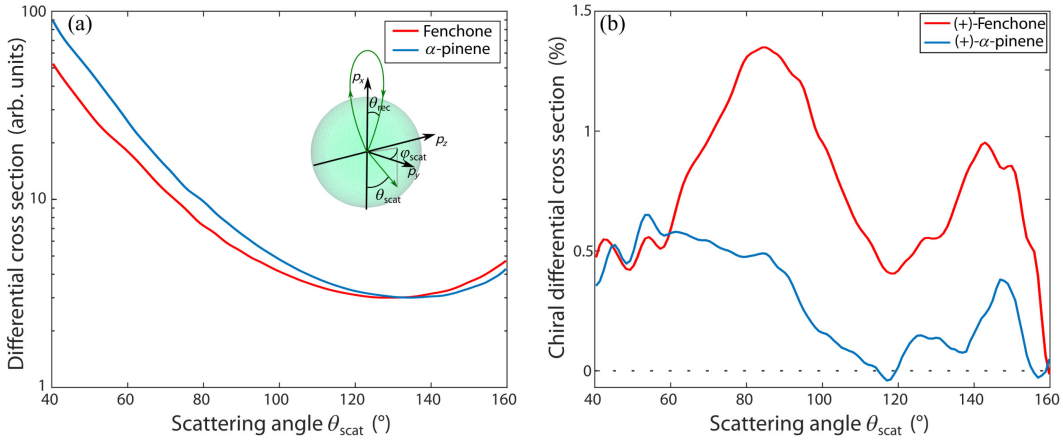

FIG. 8. Differential cross sections in chiral electron-molecule scattering. (a) Differential cross section resulting from the scattering of laser-driven electrons with 5.5–8 eV energy in (+)-fenchone (red line) and (+)-α-pinene (blue line), using a laser ellipticity $\varepsilon = 0.3$, for which the recollision angle is $\theta_{\mathrm{rec}} \approx 4°$. The DCS is integrated over $\varphi_{\mathrm{scat}} = [0:2\pi]$. (b) Chiral DCS (CDCS) obtained by differentiating the DCS from electron scattered forward and backward relative to the laser propagation direction and normalizing by the DCS.

a similar asymmetry in fenchone, but an opposite asymmetry in α-pinene. Orientational effects are known to play an important role in chiral photoionization experiments, but could up to now only be revealed by coincidence electron-ion spectroscopy [99–101]. The use of elliptically polarized strong laser fields enables us to select a set of molecular orientations and to manipulate and identify the recollision direction of the electron with the parent ion.

Laser-induced electron diffraction experiments are often analyzed by extracting the differential cross section as a function of the electron scattering angle. In our measurements the ellipticity of the laser field and the chirality of the target make the DCS depend on the azimuthal φ_{scat} and polar θ_{scat} coordinates of the rescattered electron momentum, represented in the inset of Fig. 8. These coordinates are defined with respect to the direction of the main axis of the laser polarization ellipse ($\hat{\mathbf{e}}_{\mathrm{x}}$). To reduce the dimensionality of the measurement, we plot in Fig. 8(a) the DCS integrated over all φ_{scat}. We focus here on first-return electrons, because they originate from a single family of electron trajectories (the long ones). Consistently with Fig. 2(c), we thus average the signal from the electrons recolliding with kinetic energies between $2.2U_P$ and $3.17U_P$. The DCS are normalized to their minimum value. The results obtained in fenchone (red line) and α-pinene (blue line) show a decay of more than one order of magnitude as the scattering angle increases from 40° to 130°, followed by a slight increase. The fenchone DCS minimizes at $\theta_{\mathrm{scat}} = 130°$, while in α-pinene the minimum is at $\theta_{\mathrm{scat}} = 138°$. Despite this subtle difference, the overall structures of the two DCSs are very similar. This is due to the fact that the de Broglie wavelength of the recolliding electrons (~4–5 Å) is too large to resolve the internuclear distances in the molecules, which are on the order of 1.5 Å. Indeed, laser-induced electron diffraction experiments generally use higher-energy electrons, typically in the 100 eV range, to resolve such bond lengths. In our experiment the long duration of the laser pulses (130 fs) prevents us access to such de Broglie wavelength, because of the saturation of the ionization process with increasing laser intensity.

To determine the chiral sensitivity of the electron diffraction process, we compare the DCS measured forward ($\varphi_{\mathrm{scat}} \in [0, \pi]$) and backward ($\varphi_{\mathrm{scat}} \in [\pi, 2\pi]$) along the light propagation axis, and introduce the chiral DCS (CDCS) as

$$\mathrm{CDCS}(p, \theta_{\mathrm{scat}}) = \frac{\int_0^{\pi} \mathrm{DCS}(p, \theta_{\mathrm{scat}}, \varphi_{\mathrm{scat}}) d\varphi_{\mathrm{scat}} - \int_{\pi}^{2\pi} \mathrm{DCS}(p, \theta_{\mathrm{scat}}, \varphi_{\mathrm{scat}}) d\varphi_{\mathrm{scat}}}{\int_0^{\pi} \mathrm{DCS}(p, \theta_{\mathrm{scat}}, \varphi_{scat}) d\varphi_{\mathrm{scat}} + \int_{\pi}^{2\pi} \mathrm{DCS}(p, \theta_{\mathrm{scat}}, \varphi_{\mathrm{scat}}) d\varphi_{\mathrm{scat}}}. \quad (5)$$

The results are displayed in Fig. 8(b) for a laser ellipticity $\varepsilon = 0.3$. In (+)-fenchone the CDCS maximizes at 1.2% around $\theta_{\mathrm{scat}} = 84°$, minimizes at $\theta_{\mathrm{scat}} = 118°$, shows a secondary maximum around $\theta_{\mathrm{scat}} = 143°$ before decaying to zero at $\theta_{\mathrm{scat}} = 160°$. In (+)-$\alpha$-pinene, the CDCS is about 0.5% between $\theta_{\mathrm{scat}} = 40°$ and 85°, and drops as the scattering angle further increases to reach zero around 110° before reincreasing. The CDCS from opposite enantiomers are opposite. These results show that the CDCS, associated with the chiral laser-induced electron diffraction process, has a good structural sensitivity, being able to clearly distinguish fenchone and α-pinene.

B. Simulations

We now aim at modeling the experiment, focusing on the (+)-fenchone measurements. We use the quantitative rescattering (QRS) formulation of LIED [43,55,102,103], which follows the intuitive process described above: For each molecule within the sample, the rescattered electron distribution consists of the product of the returning electron wave packet and the field-free electron-ion DCS. The amplitude of the returning wave packet is determined by the orientation-dependent ionization rate $W(\Omega_{\rm mol})$. We assume that ionization occurs as the electric field peaks about the major axis of its ellipse and therefore employ the molecular orbital Ammosov-Delone-Krainov rate displayed in Fig. 3. This rate is associated to strong-field ionization from the HOMO of fenchone. We investigated the contribution from deeper orbitals, and found that the ionization rate from the HOMO-1 orbital remains below ∼3% of that of the HOMO, due to its larger ionization potential. Therefore, the ionization from deeper orbitals can safely be neglected.

The total rescattered electron distribution is given by the averaged sum of individual molecular contributions $\Omega_{\rm mol}$ within the sample:

$$\mathrm{DCS}(\theta_{\rm rec},p,\theta_{\rm scat},\varphi_{\rm scat}) = \frac{1}{8\pi^2}\int d\Omega_{\rm mol}\, W(\Omega_{\rm mol})\sigma(\theta_{\rm rec},\Omega_{\rm mol},p,\theta_{\rm scat},\varphi_{\rm scat}), \quad (6)$$

where $\sigma(\theta_{\rm rec},\Omega_{\rm mol},p,\theta_{\rm scat},\varphi_{\rm scat})$ is the differential cross section for elastic scattering of electrons impinging on the fenchone cation with recollision angle $\theta_{\rm rec}$. The nuclei are assumed to remain frozen at the equilibrium geometry of the neutral target throughout the interaction. We checked that the equilibrium geometry of the fenchone cation is very close to the geometry of the neutral, which is due to the structural rigidity inherent to the bicyclic carbon ring of the molecule [104]. Therefore, the frozen nuclei assumption is valid in spite of the few femtoseconds the electron takes to return onto the ionic core after ionization. In LIED studies, the elastic scattering cross section is generally derived from the independent atom model (IAM) [105], where the molecule is described as a set of noninteracting atoms. This rather coarse approximation yields accurate enough DCS when the energy of the impinging electron is typically higher than ∼100 eV (see, e.g., Ref. [43]). Therefore, calculations based on the IAM are well suited to the description of LIED involving midinfrared lasers with large U_P (see, e.g., Refs. [45,54]). Here we deal with a 1030 nm driving laser operating at $\sim 2.5\times10^{13}$ W cm^{-2}, which corresponds to $U_P\sim 2.5$ eV and maximum returning electron energies of ∼8 eV. In this energy range, the genuine molecular character of the target, i.e., the electron delocalization allowing for chemical bonding throughout molecular orbitals, is essential, so that the IAM is not valid. We thus implement quantitative rescattering calculations using a higher level of theory for electron-ion collisions, based on the R-matrix formalism [106]. The differential cross section is given by [107]

$$\sigma(\theta_{\rm rec},\Omega_{\rm mol},p,\theta_{\rm scat},\varphi_{\rm scat}) = |f_{\rm C}(\theta_{\rm rec},p,\theta_{\rm scat},\varphi_{\rm scat}) + f_{\rm SR}(\theta_{\rm rec},\Omega_{\rm mol},p,\theta_{\rm scat},\varphi_{\rm scat})|^2, \quad (7)$$

where $f_{\rm C}$ is the scattering amplitude associated to the asymptotic Coulomb behavior $-1/r$ of the interaction, and $f_{\rm SR}$ is its short-range counterpart. $f_{\rm C}$ does not depend on molecular orientations while $f_{\rm SR}$ includes the molecular anisotropic features of the target—including its chirality—and therefore depends on $\Omega_{\rm mol}$. The short-range amplitude has been computed in the framework of the R-matrix approach [108] using the UKRmol+package [109], as detailed in the Appendix D.

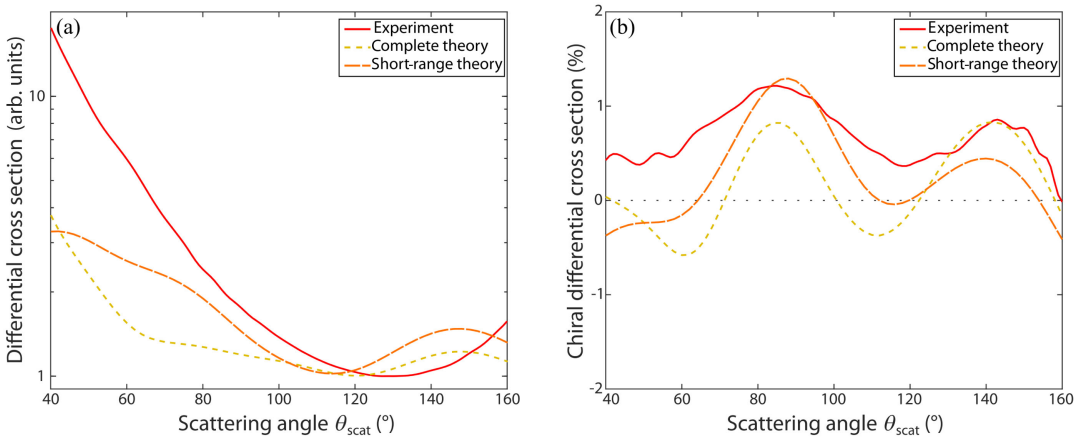

FIG. 9. Simulations of chiral electron-molecule scattering. Comparison between experimental (red continuous line) and theoretical DCS (a) and CDCS (b), resulting from the scattering of laser-driven electrons with 5.5–8 eV energy in (+)-fenchone using the full potential (yellow dotted line) and the short-range potential (orange dashed line), with a recollision angle of 4°.

We compare the results of our simulations for $\theta_{\mathrm{rec}} = 4°$ with experiments in (+)-fenchone in Fig. 9. We focus on diffraction patterns resulting from electron trajectories belonging to the first long return family, with energies between 5.5 and 8 eV. Therefore, both the experimental and theoretical results have been averaged over this energy range. The orientation average in Eq. (6) is evaluated as a numerical quadrature over molecular orientations described by Euler angles (α, β, γ) [110] with angle spacing $\Delta\alpha = \Delta\beta = \Delta\gamma = \pi/14$ rad, for which the convergence of the computed DCS and CDCS is reached.

According to Eq. (7), the DCS is the sum of the pure Coulomb contribution $|f_{\mathrm{C}}|^2$, the short-range component $|f_{\mathrm{SR}}|^2$, and the interference between them, $2\mathcal{R}(f_{\mathrm{C}}^* f_{\mathrm{SR}})$. This sum yields a result which is in poor agreement with the measured DCS, as evidenced in Fig. 9(a). Neglecting artificially the Coulomb contribution, i.e., setting $f_{\mathrm{C}} \equiv 0$, makes the agreement of the computed and measured DCS better for $\theta_{\mathrm{scat}} \geq 80°$, in spite of a remaining shift of the computed DCS toward small angles. This behavior indicates that the scattering process at large angles is mainly determined by the short-range part of the underlying electron-ion interaction. This is consistent with the fact that large scattering angles are classically associated with small impact parameters [111]. Introducing the asymptotic Coulomb amplitude in the expression of the DCS leads to a drastic decrease of the cross section for $\theta_{\mathrm{scat}} < 100°$, induced by the interference term $2\mathcal{R}(f_{\mathrm{C}}^* f_{\mathrm{SR}})$. The simulations thus seem to overestimate the (destructive) interference between the Coulomb and short-range components. In this respect, the Coulomb amplitude refers to a totally screened molecular ion. However, we observe in Fig. 2(c) that the field-induced electron trajectories reach a maximal distance of ∼15 a.u. from the origin of the molecule, whose skeleton extends over ∼8 a.u. In other words, the freed electron does not go far enough to reach an area where the molecular ion potential is totally screened off when it begins to return toward the core. Partial screening and antiscreening effects have been largely studied in fast ion-atom collisions (see, e.g., Refs. [112,113]). They cannot be rationalized in the present quantitative rescattering context which employs a stationary formulation of the underlying electron-ion interaction with fixed $-1/r$ asymptotic behavior. On the other hand, our simulations take into account only the long trajectories of first returns. However, high-energy third returns can participate in the diffraction (see Fig. 14) even if their weight, integrated between 5.5 and 8 eV, is smaller than that of long first pathways. Disregarding these multiple returns could be an additional source of discrepancy between theory and experiment.

We compare the computed chiral DCS, using full or short-range calculations, with their experimental counterpart in Fig. 9(b). The general agreement with the measurements is much more satisfactory than for the DCS. This points to the negligible influence of third returns on the CDCS, because of their small recollision angles, and predominance of long first returns in the chiral signal. The overall sign and magnitude of the theoretical CDCS match the ones measured in the experiment. The computed CDCS consists of two main peaks. Interestingly, their locations coincide better with the measurements when the interference term between the Coulomb and short-range components of the scattering amplitude is explicitly taken into account—$|f_{\mathrm{C}}|^2$ plays no role in the CDCS. Interferences shift the first maximum from 88° to 85° while the second maximum is upshifted from 140° to 142°. These values are in good agreement with the experimental ones, which are 84° and 143° for the first and second maxima, respectively. Concerning the magnitude of the CDCS, the full calculations slightly underestimate it around the first maximum, yielding 0.82% (versus 1.2% in the experiment). However, the calculations reproduce quite accurately the dichroism of backscattered ($\theta_{\mathrm{scat}} > 120°$) electrons, yielding a CDCS of 0.83% at the top of the second maximum (versus 0.9% in the experiment).

These results allow us to state that chiral LIED simulations based on QRS description and underlying R-matrix calculations capture the main features observed in the measurements. This leads us to conclude that in spite of the difficulties inherent to low-energy electron rescattering, LIED using rather small ponderomotive energies enables us to self-image chiral molecules.

VII. CONCLUSION

Our results have revealed the ability of elliptically polarized strong laser fields to probe molecular chirality, relying on three key elements: (i) the selective ionization of a subset of molecules, acting as an orientation filtering, (ii) the manipulation of the electron trajectories through the laser field ellipticity, and (iii) the chirosensitive differential scattering of the laser-accelerated electrons by the oriented molecule. This process leads to strong forward-backward asymmetries in the photoelectron angular distributions of the recollided electrons. Identifying the electron trajectories through the ellipiticity dependence of the electron yield has enabled us to assign first and second returns, corresponding to collisions from opposite sides of the molecule. In α-pinene, these opposite recollisions induce opposite forward-backward asymmetries. The electron-molecule collisions can be analyzed to extract angle-resolved differential cross sections, which are found to be different in the forward and backward directions with respect to the laser polarization plane, as a result of the chiral nature of the target molecules. While the measured DCS is hardly able to distinguish fenchone and α-pinene molecules, their chirosensitive responses, encoded in the chiral DCS, are drastically different.

To understand the enhanced structural sensitivity of the CDCS compared to the DCS, let us consider another research field where electron scattering plays a crucial role: x-ray absorption near-edge spectroscopy (XANES) in condensed matter. The absorption of x rays above an atomic ionization edge releases electrons that can scatter off neighbors and recombine to the ground state, leading to modulations of the absorption spectrum. Fourier transforming the spectrum provides the typical bond length of the neighboring atoms in the medium. If the target is chiral, additional information can be obtained by using circularly polarized x rays to measure x-ray natural circular dichroism (XNCD) [114]. The XNCD spectrum typically shows faster modulations in energy range, which correspond to distances larger than the bond length in the material. This is due to the fact that CD is determined by chirality, which is a nonlocal property of matter. Thus, XNCD is sensitive to multiple scattering events, and "sees" bond lengths larger than the internuclear distance between neighbors in the medium [115]. In LIED, the situation is very similar. The overall LIED signal—the DCS—is dominated by modulations imposed by the bond lengths in the molecule. Resolving these modulations requires using energetic electrons, whose de Broglie wavelength is typically around 1.5 Å. On the other hand, the chirosensitive LIED signal—the CDCS—is sensitive to the overall shape of the molecular potential, which extends over several angstrom, and can be revealed using lower-energy electrons with 4.5 Å wavelength. Similarly, one could also expect that the enhanced spectroscopic power of XNCD over XANES which has recently been theoretically demonstrated in molecular spectroscopy [116] should exist in CDCS.

Looking forward, the chiral laser-induced electron diffraction resulting from these collisions could be much enhanced by using longer laser wavelengths, which will produce electrons with much shorter de Broglie wavelengths [117]. Prealigning the target molecules [78,79] could further increase the anisotropy of the interaction [118] and the sensitivity of the technique. Alternatively, detecting the ionic fragments in coincidence with the electrons could enable disentangling the possible contributions of different sets of aligned molecules [119] associated with different molecular orbitals [101].

The possibility to observe chirosensitive effects in electron-ion collisions without relying on spin polarization constitutes an important fundamental step—the electrons do not need to be spin polarized to give rise to chiral laser-induced electron diffraction. This does not mean that spin cannot induce additional effects in the process. Strong-field ionization naturally produces spin-polarized electrons [120,121]. Resolving the spin of both the impinging and diffracted electrons could provide important insights into the mechanism of chiral-induced spin selectivity [122–124], which is at the heart of many applications, from chemistry to spintronics [125], but whose fundamental origin remains debated.

ACKNOWLEDGMENTS

We thank R. Bouillaud, F. Blais, N. Fedorov, and L. Merzeau for technical assistance. This project has received funding from the Agence Nationale de la Recherche (ANR)—Shotime (ANR-21-CE30-038-01), from the European Research Council (ERC) under the European Union's Horizon 2020 research and innovation programs No. 682978—EXCITERS, No. 864127—ATTOGRAM, and from No. 871124—Laserlab-Europe.

APPENDIX A: HIGH-HARMONIC SPECTROSCOPY INVESTIGATION OF STRONG-FIELD-INDUCED MOLECULAR ORIENTATION

We employ high-harmonic spectroscopy to show that strong-field ionization induces molecular orientation within a sample of randomly oriented molecules, breaking the symmetry of the light-sample interaction. In an isotropic medium, a linearly polarized laser field produces linearly polarized high harmonics: the polarization of the harmonics is parallel to the recollision direction of the electrons. If the laser field is elliptically polarized, the recollision direction of the electron is tilted with respect to the main axis of the laser ellipse. If the generating medium is isotropic, then the polarization direction of the harmonics is still determined by this recollision direction only, as illustrated in Fig. 10(a). Consequently, any deviation of the harmonic polarization from this direction is a signature of symmetry breaking in the generating medium [Fig. 10(b)]. Such symmetry breaking was, for instance, detected by comparing the polarization states of high harmonics from randomly aligned and aligned diatomic molecules [87], or between He atoms, whose $1s$ orbital is isotropic, and Ne atoms, whose $2p$ orbital is aligned by strong-field ionization [88].

In our experiment, we focused 70 fs pulses centered at 1850 nm into gaseous fenchone molecules. We used the 1 kHz Ti:sapphire laser system Aurore at CELIA [126], which delivers 8 mJ, 27 fs pulses at 800 nm. The laser pulses were frequency converted in a noncollinear parametric amplifier (HE TOPAS) to produce 700 μJ, 70 fs pulses at 1850 nm. The laser ellipticity was controlled by a zero-order half wave plate in front of a fixed quarter wave plate. The laser was focused by a $f = 37.5$ cm focal lens in a heated gas cell containing gaseous fenchone molecules at a pressure around 100 mbar. The generated high-order harmonics were dispersed by a 1200 mm^{-1} variable groove spacing grating and imaged by a set of microchannel plates, a phosphor screen, and a CCD camera. A set of three bare gold mirrors was placed between the generation cell and the XUV spectrometer to act as an XUV polarization analyzer, reflecting ∼70 times more vertically than horizontally

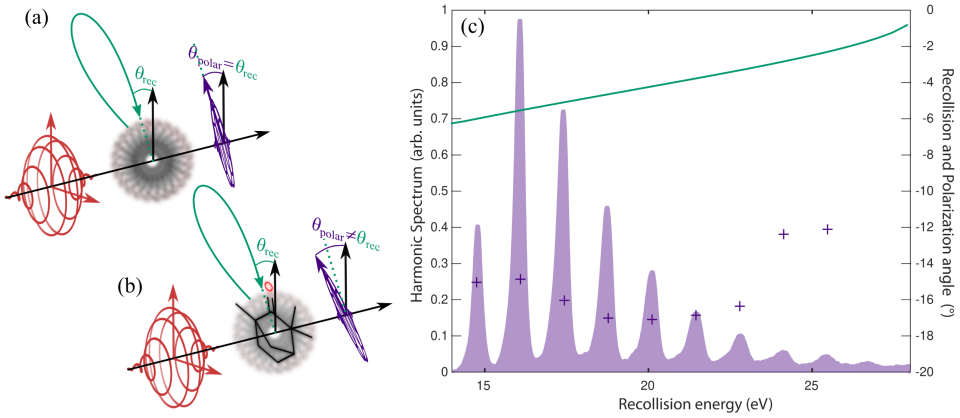

FIG. 10. Molecular orientation selection in strong-field ionization. (a) In an isotropic medium, an elliptically polarized laser pulse generates high-order harmonics polarized along the recollision direction of the electrons. (b) If strong-field ionization breaks the isotropy of the medium by preferentially selecting a subset of oriented molecules, the polarization direction of the harmonics will deviate from the recollision direction. (c) Experimental spectrum (filled area) and polarization direction (crosses) of high-order harmonics generated in (+)-fenchone molecules by a 1850 nm laser field at 3×10^{13} W cm^{-2} with $\varepsilon = 0.15$ ellipticity. The green line is the simulated recollision angle of the electrons for the short trajectories, which are macroscopically selected in the HHG process.

polarized XUV radiation. The polarization direction of the harmonics was determined by recording Malus's laws, rotating a zero-order half wave plate in the laser beam to control the polarization direction of the radiation with respect to the fixed analyzer.

Figure 10(c) shows the harmonic spectrum generated at $\sim 3 \times 10^{13}$ W cm^{-2} laser intensity with a laser ellipticity $\varepsilon = 0.15$. The ponderomotive potential of the laser field is $U_P \sim 9.6$ eV. The ionization potential of fenchone is $Ip = 8.7$ eV. The Keldysh parameter, which characterizes the ionization regime, is thus $\gamma = \sqrt{Ip/2U_P} \sim 0.7$, indicating that the experiment takes place in the tunneling regime ($\gamma < 1$) rather than in the multiphoton regime where $\gamma \gg 1$. The measured spectrum extends from harmonic 35 to harmonic 53. These harmonics are produced by electrons that recollide with a kinetic energy ranging from 14.7 to 26.8 eV.

As we saw in Sec. II, a number of different recolliding electron trajectories could in principle lead to the high-order harmonic emission. However, it is well established that experimentally the high-order harmonic emission is dominated by the contributions of first returns. Furthermore, the experimental conditions are often optimized to maximize the macroscopic contribution from short trajectories, which are easier to phase match. This is the case in this study, where the spectrally narrow harmonics measured in Fig. 10(c) are typical of short trajectories [127,128]. The calculated classical recollision angles of the electrons producing these short harmonics are shown in Fig. 10(c) (green line). The role of the ionic potential on the electron motion was neglected in the calculation, as previous studies have shown that it has a negligible influence on the recollision angles for short trajectories [68]. The measured polarization angles (purple crosses) are clearly offset with respect to the theoretical recollision direction (green line), being systematically more than 8° away from it. The recollision angle monotonically increases as the harmonic order increases. By contrast, the polarization angle of the harmonics decreases between 15 and 20 eV recollision energy, before increasing for higher harmonics.

Drawing from the comparison of harmonic signals emitted by randomly oriented and aligned diatomics [87], the offset of the harmonic polarization angle with respect to the recollision angle is also attributed here to a clear anisotropy in the tunnel ionization process: The recolliding electrons see a set of partially oriented molecules.

APPENDIX B: MEASUREMENT OF 3D PHOTOELECTRON ANGULAR DISTRIBUTIONS

The photoelectron imaging measurements were conducted using the BlastBeat laser system at CELIA (dual Tangerine Short Pulse, Amplitude). The laser delivers 130 fs pulses centered at 1030 nm, with 50 W average power. The repetition rate was set to 1 MHz. The laser beam was attenuated by a half wave plate followed by a thin film polarizer. The polarization state of the beam was further cleaned after all reflections carrying the beam to the experiment using another thin film polarizer (see Fig. 11). The linearly polarized light was then incident onto a zero-order half wave plate (Bernhard Halle) which was mounted on a continuously rotating direct-drive mount (Newport RGV100BL), followed by a zero-order quarter wave plate (Bernhard Halle). The polarization state of the laser beam after the quarter wave plate was measured using a rotating quarter wave plate polarimeter, for different orientations of the laser polarization with respect to the fast axis of the quarter wave plate. The third Stokes parameter was found

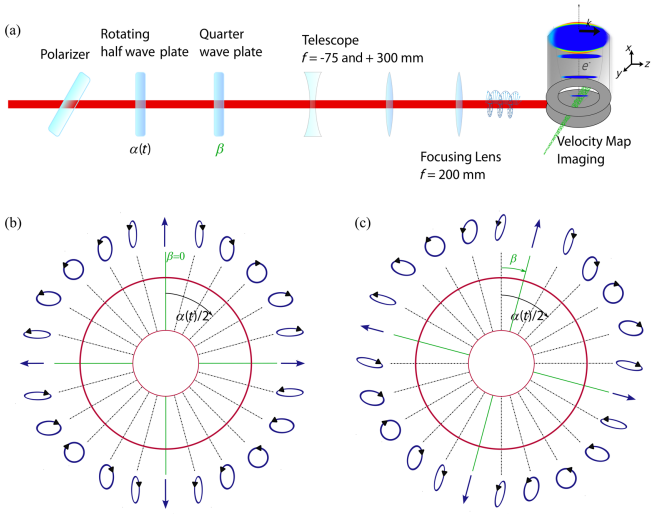

FIG. 11. (a) Experimental setup for the measurement of 3D photoelectron angular distributions. (b) Evolution of the polarization state of the ionizing radiation as the half wave plate rotates, when the quarter wave plate axis is vertical. (c) Same after rotating the quarter wave plate by β, to record a different set of projections of the photoelectron angular distribution.

to be 0.00 for the linear polarizations and $|S_3| = 0.99$ for both left and right circular polarizations. The beam was then expanded using a ×4 telescope (constituted of lenses with −75 and +300 focal lengths) before being focused into the velocity map imaging (VMI) spectrometer using a +200 mm focusing lens. The focal spot size was measured using a CCD camera and had a FWHM of 18 μm.

The VMI consists of three electrodes—repeller, extractor, and ground—forming an electrostatic lens that images the velocity distribution of the electrons onto a set of dual microchannel plates imaged by a fast phosphor screen (P47) and a S-CMOS camera (Orca Flash 4.0, Hamamatsu). The VMI is shielded by a μ-metal cylinder, and an additional set of Helmoltz coil was used to compensate for stray magnetic fields that may penetrate by the end of the μ-metal cylinder. The enantiopure molecules were introduced through a stainless-steel heated gas line (at 90°) until a 200 μm nozzle followed by a 1 mm skimmer placed 7 cm away from the laser focus. No carrier gas was used.

The data acquisition was conducted by continuously filming the phosphor screen in the VMI while rotating the half wave plate. The exposure time of the camera was set to 50 ms, which corresponds to the accumulation of 50 000 laser shots and was enough to measure a 2D projection of the 3D photoelectron momentum distribution with good signal-to-noise ratio. The acquisition was performed at a rate of 20 Hz with no dead time. As the half wave plate rotates at a constant speed of 22.5°/s, the polarization state of the light emerging from the quarter wave plate periodically oscillates between linear and circular, the polarization ellipse direction periodically switching from the slow to the fast axis of the quarter wave plate, as depicted in Fig. 11(b). This scheme thus enables us record two projections of the photoelectron momentum distribution produced by a given ellipticity. Since the detected signal is periodic, the signal-to-noise ratio of the measurements can be improved by performing a Fourier filtering. We first symmetrize the images along the vertical dimension, and separate them in two components: a symmetric component along the laser propagation direction and an antisymmetric component along this direction. We then Fourier transform the temporal evolution of each pixel of the camera and extract the 2D Fourier components at the different frequencies, shown in Fig. 12. The fundamental frequency Ω_0 of the experiment corresponds to a rotation of 180° of the half wave plate, i.e., $\Omega_0 = 0.125$ Hz. We then inverse Fourier transform these components to retrieve the filtered evolution of the photoelectron angular distribution as a function of the half wave plate rotation. This operation is repeated for successive angular positions β of the quarter wave plate [Fig. 11(c)], enabling us to record a set of 72 projections of the 3D momentum distribution with an angular sampling step of 5°. The 3D distribution is then reconstructed by inverse Radon transform [93].

As described in Eq. (3), we performed acquisitions in opposite enantiomers to extract the FBA, PEELD, and CDCS presented in the article. Figure 13 shows projections of the PEELD measured in (+)-α pinene (top) and (−)-α pinene, in elliptical and circular polarization. The PEELD shows a clear sign inversion when switching enantiomer, and the main features, in particular the opposite PEELD from first- and second-return electrons, are observed in both enantiomers. The detailed shapes of these structures are slightly different because of residual artifacts in the photoelectron imaging. This is what led us to systematically work on differential signals using the two enantiomers, as defined in Eq. (3).

APPENDIX C: CTMC CALCULATIONS

CTMC calculations have been run to assess the influence of the ionic potential on the dynamics of recolliding electrons. We considered a monoelectronic atomic system with nuclear charge $Z = 0.8$, whose fundamental state has the same ionization potential as fenchone. As detailed in Refs. [129,130], CTMC employs a phase-space distribution, discretized in terms of $\mathcal{N}$ noninteracting trajectories, to describe classically the electron dynamics subject to both the target and laser potentials. The initial distribution, representing the unperturbed atomic state, consists of a so-called hydrogenic distribution [131,132] which provides an accurate representation of the tail of the quantal electron density in coordinate space, beyond the usual microcanonical framework. Such an improved distribution is known to lead to a better description of ionization processes [133]. We employed $\mathcal{N} = 10^7$ trajectories.

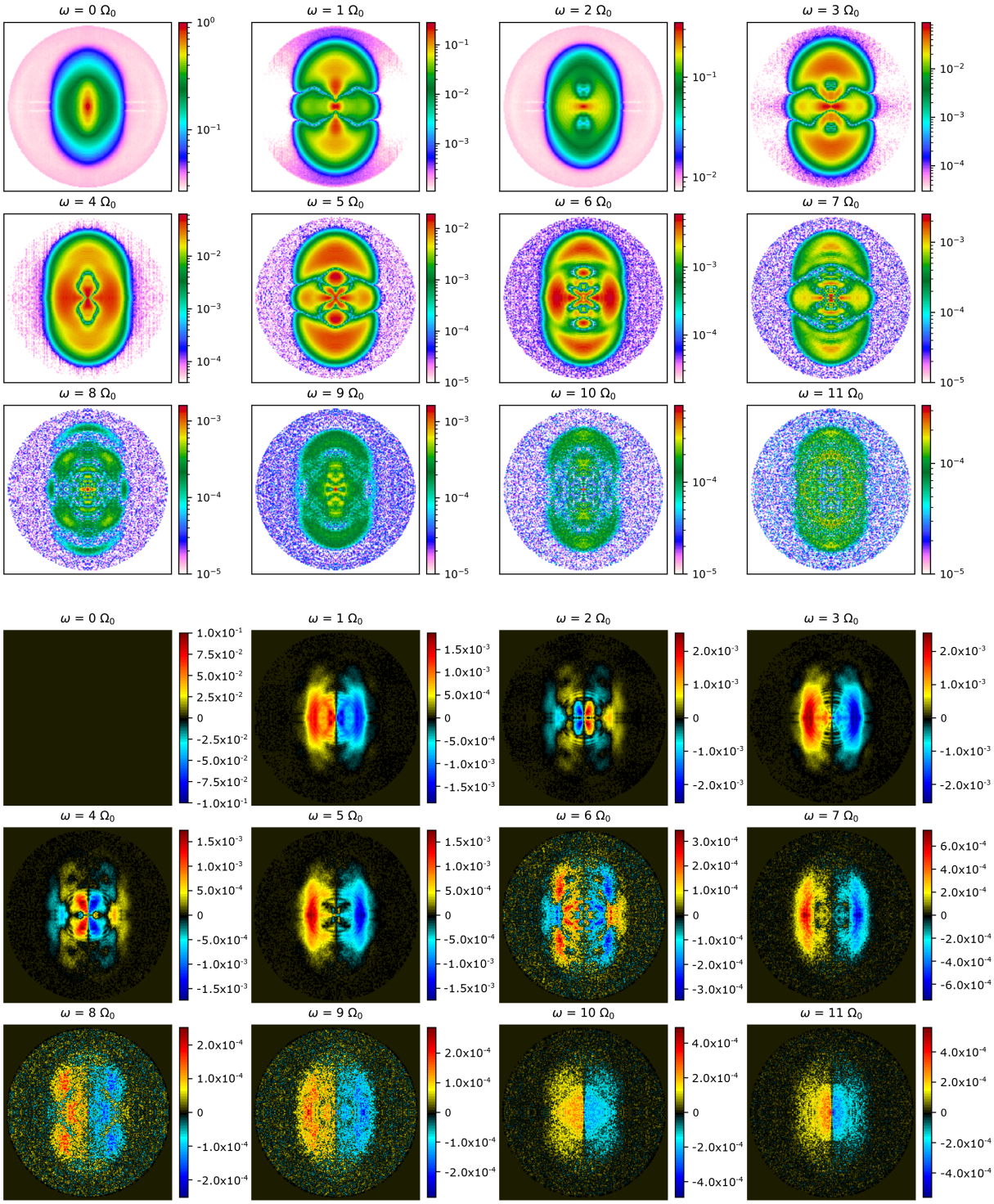

FIG. 12. Fourier components of the symmetric (top) and antisymmetric (bottom) photoelectron images.

In the course of the interaction with the laser pulse, the electron trajectories are identified as they leave a spherical box of radius $r_0 = 7$ a.u. centered on the nucleus—the electron density extends up to $r \sim 5$ a.u. in the initial state. Recolliding trajectories reenter the box later on, and single and multiple returns, as well as long and short trajectories, are discriminated in terms of their time of flight between ionization and recollision [75].

The electron energy at time of recollision is presented in Fig. 14 for a laser pulse with $I = 2.5 \times 10^{13}$ W/cm^2, $\lambda = 1030$ nm, and $\varepsilon = 0.3$. The results of the Coulomb-free classical calculations (black lines) are also included in

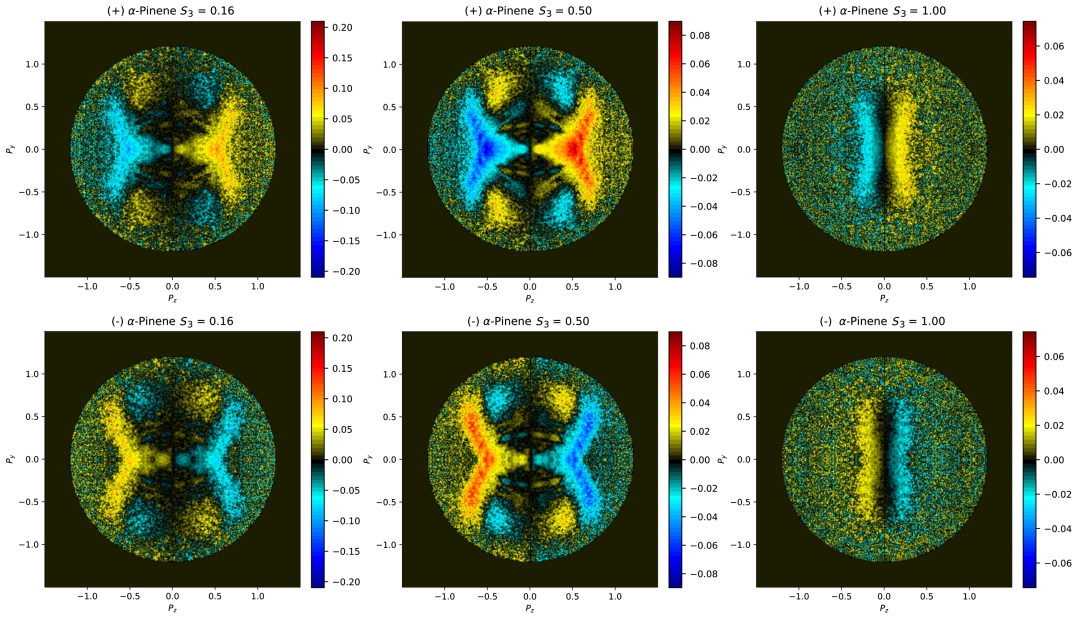

FIG. 13. Projections in the (x, z) plane of the PEELD measured in $(+)$-α pinene (top) and $(-)$-α pinene (bottom), for three different laser ellipticities.

the figure to gauge the role of the target potential. The most striking feature of Fig. 14 is the lack of long third returns in the CTMC framework. A similar feature showed up in the semiclassical calculations of Hao *et al.* [75] who submitted Ar atoms to a linearly polarized pulse with $I = 1.25 \times 10^{14}$ W/cm^2 at $\lambda = 800$ nm. The lack of long third returns can be understood with the help of the trajectories displayed in Fig. 2(f): During their travel between ionization and recollision, third long trajectories present a first impact parameter (distance of closest approach to the core in the y direction) twice as small as those associated to short trajectories. They are thus strongly deflected by the central potential, prohibiting their next recollision. This mechanism has been referred to as Coulomb defocusing in Refs. [134,135]. Trajectories with large impact parameters continue their route, guided by the field, and the Coulomb potential influences their subsequent motion by focusing them toward the core. Therefore, such trajectories end up their travel with a recollision angle smaller than its Coulomb-free counterpart, as evidenced in Figs. 2(g) and 2(h) for third long returns.

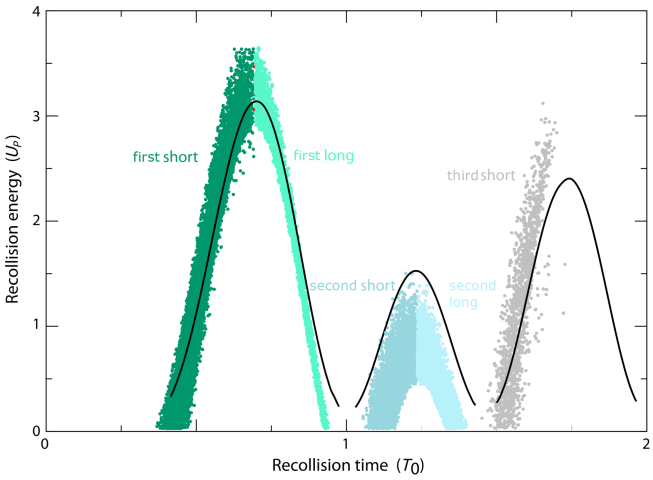

FIG. 14. Recollision energy (in units of laser ponderomotive energy) as a function of the recollision time (in units of laser period) for a pulse with $I = 2.5 \times 10^{13}$ W/cm^2, $\lambda = 1030$ nm, and $\varepsilon = 0.3$. Scattered points, CTMC calculations; line, Coulomb-free classical calculations.

The Coulomb potential also affects the timing and energy of returning electrons, as it can be expected from the classical equations of motion and discussed in, e.g., Refs. [75,136,137]: The energy cutoff of third-return electrons is significantly increased with respect to the Coulomb-free result, while the maximal energy of the second returns is slightly decreased as shown in Fig. 14.

APPENDIX D: COMPUTATION OF THE COULOMB AND SHORT-RANGE AMPLITUDES

The spherical angles $(\theta_{\rm scat}, \varphi_{\rm scat})$ characterizing scattering in the laboratory frame of reference are illustrated in the inset of Fig. 8(a) of the main text. The scattering can alternatively be rationalized in the recollision frame of reference, involving (θ, φ) angles, where the quantization axis is chosen along the incoming recollision direction. This latter frame is particularly well suited to the Coulomb scattering amplitude that reads $f_{\rm C}(p,\theta) = \exp\{2i\sigma_0^C(p) + (i/p)\ln[\sin^2(\theta/2)]\}/2p^2\sin^2(\theta/2)$ [111], where $\sigma_0^C(p) = \arg[\Gamma(1 - i/p)]$, $\Gamma(x)$ standing for the Gamma function [138]. The recollision frame is obtained by rotating the

laboratory frame by $\theta_{\rm rec}+\pi$ around the x axis [see Fig. 8(a)]. Therefore, $\theta=\cos^{-1}[\cos(\theta_{\rm rec})\cos(\theta_{\rm scat})-\sin(\theta_{\rm rec})\sin(\theta_{\rm scat})\cos(\varphi_{\rm scat})]$ and $f_{\rm C}(p,\theta)\equiv f_{\rm C}(\theta_{\rm rec},p,\theta_{\rm scat},\varphi_{\rm scat})$.

The expression of the short-range amplitude is derived from the seminal paper of Dill and Dehmer [139], involving the partial-wave decomposition of the outgoing scattering state onto spherical waves with (l,m) orbital momenta:

$$f_{\rm SR}(\theta_{\rm rec},\Omega_{\rm mol},p,\theta_{\rm scat},\varphi_{\rm scat})=-\frac{2i\pi}{p}\sum_{ll'mm'}i^{l-l'}e^{i[\sigma_l^C(p)+\sigma_{l'}^C(p)]}[S_{lml'm'}(p)-\delta_{ll'}\delta_{mm'}]\times\sum_{m''}D^{l^*}_{m''m}(\Omega_{\rm mol})Y_l^{m''*}(\theta_{\rm rec},\varphi_{\rm rec})\sum_{m'''}D^{l'}_{m'''m'}(\Omega_{\rm mol})Y_{l'}^{m'''}(\theta_{\rm scat},\varphi_{\rm scat}). \tag{D1}$$

$D^{l_1}_{m_1m_2}$ and $Y^{m_1}_{l_1}$ are Wigner rotation matrices and spherical harmonics [110], respectively, and $\sigma_l^C(p)=\arg[\Gamma(l+1-i/p)]$ is the Coulomb phase shift for orbital momentum l [111]. $S_{lml'm'}(p)$ are the S-matrix elements, characterizing the complex magnitude of scattering of outgoing spherical waves with $(l'm')$ momenta from the ingoing spherical wave defined by (l,m). For the rescattering associated with long trajectories of first returns, $\varphi_{\rm rec}=\pi$ to simulate experiments with $\varepsilon\geq 0$ while $\varphi_{\rm rec}=0$ for $\varepsilon<0$.

The S-matrix elements are computed in the framework of the R-matrix approach [108] using the UKRmol+package [109]. The equilibrium geometry of neutral fenchone, belonging to the C_1 point group, was obtained using density functional theory [140] with the hybrid B3LYP functional [141,142] and the 6-311++G(dp) Gaussian basis [143,144]—Hartree-Fock calculations with the same basis yield an almost identical structure. The R-matrix scattering calculations are performed within the static-exchange (SE) approximation in which the multielectronic ground state wave function of the fenchone cation is described using a single Slater determinant. The Hartree-Fock orbitals used are obtained with the double zeta + polarization basis set [145,146]. Use of this basis set ensures the electronic density associated to the ground state is contained in an inner region defined by an R-matrix sphere of radius of $r_{\rm max}=13a_0$. In this region, two types of electronic configurations of neutral fenchone are built by placing the scattering electron in (i) a "continuum orbital" built from Gaussian functions placed at the center of mass of the system and (ii) a virtual (unoccupied) molecular orbital. Singlet symmetry is enforced for the neutral target since the electron flight associated to first return electron trajectories (3.5 fs at most) is too short to allow for spin flip during the interaction. The maximum continuum angular momentum $l_{\rm max}=6$, yielding 396 continuum orbitals, and 10 virtual orbitals are used; this gives a total of 407 configurations. The neutral fenchone wave functions in the outer region, whose asymptotic form is analytically known, are matched at $r_{\rm max}$ with the inner region multielectronic wave functions. Propagation and matching with the asymptotic solutions [109] provides the energy-dependent K matrix that can be trivially transformed into the required S matrix.

Calculations at the static-exchange plus polarization level, in which single excitations from the ground state configuration of the cation are allowed, using a small number of virtual orbitals (up to 20) showed negligible differences with the SE results. Similarly, increasing the maximum continuum angular momentum to $l_{\rm max}=7$ did not lead to significant changes in the differential cross sections.

[1] William A. Bonner, *Chirality and life*, Origins Life Evol. Biosphere **25**, 175 (1995).

[2] L. Keszthelyi, *Origin of the homochirality of biomolecules*, Q. Rev. Biophys. **28**, 473 (1995).

[3] N. Berova and R. Nakanishi, *Circular Dichroism Principles and Applications* (Wiley-VCH, New York, 2000).

[4] Laurence A. Nafie, *Infrared and Raman vibrational optical activity: Theoretical and experimental aspects*, Annu. Rev. Phys. Chem. **48**, 357 (1997).

[5] Malte Oppermann, Benjamin Bauer, Thomas Rossi, Francesco Zinna, Jan Helbing, Jérôme Lacour, and Majed Chergui, *Ultrafast broadband circular dichroism in the deep ultraviolet*, Optica **6**, 56 (2019).

[6] P. Fischer and F. Hache, *Nonlinear optical spectroscopy of chiral molecules*, Chirality **17**, 421 (2005).

[7] Julia Meyer-Ilse, Denis Akimov, and Benjamin Dietzek, *Recent advances in ultrafast time-resolved chirality measurements: Perspective and outlook*, Laser Photonics Rev. **7**, 495 (2013).

[8] Malte Oppermann, Francesco Zinna, Jérôme Lacour, and Majed Chergui, *Chiral control of spin-crossover dynamics in Fe(II) complexes*, Nat. Chem. **14**, 739 (2022).

[9] Lykourgos Bougas, Joseph Byron, Dmitry Budker, and Jonathan Williams, *Absolute optical chiral analysis using cavity-enhanced polarimetry*, Sci. Adv. **8**, eabm3749 (2022).

[10] Anne Zehnacker and Martin A. Suhm, *Chirality recognition between neutral molecules in the gas phase*, Angew. Chem., Int. Ed. **47**, 6970 (2008).

[11] Kiyoshi Ueda, Emma Sokell, Stefan Schippers, Friedrich Aumayr, Hossein Sadeghpour, Joachim Burgdörfer, Christoph Lemell, Xiao-Min Tong, Thomas Pfeifer, Francesca Calegari *et al.*, *Roadmap on photonic, electronic and atomic collision physics: I. Light–matter interaction*, J. Phys. B **52**, 171001 (2019).

[12] David Ayuso, Andres F. Ordonez, and Olga Smirnova, *Ultrafast chirality: The road to efficient chiral measurements*, Phys. Chem. Chem. Phys. **24**, 26962 (2022).
[13] Burke Ritchie, *Theoretical studies in photoelectron spectroscopy. Molecular optical activity in the region of continuous absorption and its characterization by the angular distribution of photoelectrons*, Phys. Rev. A **12**, 567 (1975).
[14] N. Böwering, T. Lischke, B. Schmidtke, N. Müller, T. Khalil, and U. Heinzmann, *Asymmetry in photoelectron emission from chiral molecules induced by circularly polarized light*, Phys. Rev. Lett. **86**, 1187 (2001).
[15] Christian Lux, Matthias Wollenhaupt, Tom Bolze, Qingqing Liang, Jens Köhler, Cristian Sarpe, and Thomas Baumert, *Circular dichroism in the photoelectron angular distributions of camphor and fenchone from multiphoton ionization with femtosecond laser pulses*, Angew. Chem., Int. Ed. **51**, 5001 (2012).
[16] Maurice H. M. Janssen and Ivan Powis, *Detecting chirality in molecules by imaging photoelectron circular dichroism*, Phys. Chem. Chem. Phys. **16**, 856 (2013).
[17] Laurent Nahon, Gustavo A. Garcia, and Ivan Powis, *Valence shell one-photon photoelectron circular dichroism in chiral systems*, J. Electron Spectrosc. Relat. Phenom. **204**, 322 (2015).
[18] S. Beaulieu, A. Ferré, R. Géneaux, R. Canonge, D. Descamps, B. Fabre, N. Fedorov, F. Légaré, S. Petit, T. Ruchon, V Blanchet, Y. Mairesse, and B. Pons, *Universality of photoelectron circular dichroism in the photoionization of chiral molecules*, New J. Phys. **18**, 102002 (2016).
[19] A. Comby, E. Bloch, C. M. M. Bond, D. Descamps, J. Miles, S. Petit, S. Rozen, J. B. Greenwood, V. Blanchet, and Y. Mairesse, *Real-time determination of enantiomeric and isomeric content using photoelectron elliptical dichroism*, Nat. Commun. **9**, 5212 (2018).
[20] Antoine Comby, Samuel Beaulieu, Martial Boggio-Pasqua, Dominique Descamps, Francois Légaré, Laurent Nahon, Stéphane Petit, Bernard Pons, Baptiste Fabre, Yann Mairesse, and Valérie Blanchet, *Relaxation dynamics in photoexcited chiral molecules studied by time-resolved photoelectron circular dichroism: Toward chiral femtochemistry*, J. Phys. Chem. Lett. **7**, 4514 (2016).
[21] Samuel Beaulieu, Antoine Comby, Baptiste Fabre, Dominique Descamps, Amélie Ferré, Gustavo Garcia, Romain Géneaux, Francois Légaré, Laurent Nahon, Stéphane Petit, Thierry Ruchon, Bernard Pons, Valérie Blanchet, and Yann Mairesse, *Probing ultrafast dynamics of chiral molecules using time-resolved photoelectron circular dichroism*, Faraday Discuss. **194**, 325 (2016).
[22] S. Beaulieu, A. Comby, D. Descamps, B. Fabre, G. A. Garcia, R. Géneaux, A. G. Harvey, F. Légaré, Z. Mašín, L. Nahon, A. F. Ordonez, S. Petit, B. Pons, Y. Mairesse, O. Smirnova, and V. Blanchet, *Photoexcitation circular dichroism in chiral molecules*, Nat. Phys. **14**, 484 (2018).
[23] Markus Ilchen, Philipp Schmidt, Nikolay M. Novikovskiy, Gregor Hartmann, Patrick Rupprecht, Ryan N. Coffee, Arno Ehresmann, Andreas Galler, Nick Hartmann, Wolfram Helml *et al.*, *Site-specific interrogation of an ionic chiral fragment during photolysis using an x-ray free-electron laser*, Commun. Chem. **4**, 1 (2021).
[24] Vít Svoboda, Niraghatam Bhargava Ram, Denitsa Baykusheva, Daniel Zindel, Max D. J. Waters, Benjamin Spenger, Manuel Ochsner, Holger Herburger, Jürgen Stohner, and Hans Jakob Wörner, *Femtosecond photoelectron circular dichroism of chemical reactions*, Sci. Adv. **8**, eabq2811 (2022).
[25] D. Faccialà, M. Devetta, S. Beauvarlet, N. Besley, F. Calegari, C. Callegari, D. Catone, E. Cinquanta, A. G. Ciriolo, L. Colaizzi *et al.*, *Time-resolved chiral x-ray photoelectron spectroscopy with transiently enhanced atomic site selectivity: A free-electron laser investigation of electronically excited fenchone enantiomers*, Phys. Rev. X **13**, 011044 (2023).
[26] S. Beaulieu, A. Comby, A. Clergerie, J. Caillat, D. Descamps, N. Dudovich, B. Fabre, R. Géneaux, F. Légaré, S. Petit, B. Pons, G. Porat, T. Ruchon, R. Taïeb, V. Blanchet, and Y. Mairesse, *Attosecond-resolved photoionization of chiral molecules*, Science **358**, 1288 (2017).
[27] David Patterson, Melanie Schnell, and John M. Doyle, *Enantiomer-specific detection of chiral molecules via microwave spectroscopy*, Nature (London) **497**, 475 (2013).
[28] Sandra Eibenberger, John Doyle, and David Patterson, *Enantiomer-specific state transfer of chiral molecules*, Phys. Rev. Lett. **118**, 123002 (2017).
[29] Sérgio R. Domingos, Cristóbal Pérez, Mark D. Marshall, Helen O. Leung, and Melanie Schnell, *Assessing the performance of rotational spectroscopy in chiral analysis*, Chem. Sci. **11**, 10863 (2020).
[30] P. K. Kabir, Gabriel Karl, and Edward Obryk, *Optical activity for neutrons*, Phys. Rev. D **10**, 1471 (1974).
[31] A. Rich, J. Van House, and R. A. Hegstrom, *Calculation of a mirror asymmetric effect in electron scattering from chiral targets*, Phys. Rev. Lett. **48**, 1341 (1982).
[32] T. L. V. Ulbricht and F. Vester, *Attempts to induce optical activity with polarized β-radiation*, Tetrahedron **18**, 629 (1962).
[33] K. Blum and D. G. Thompson, *Chiral effects in electron scattering by molecules*, in *Advances in Atomic, Molecular, and Optical Physics*, edited by Benjamin Bederson and Herbert Walther (Academic Press, New York, 1998), Vol. 38, pp. 39–86.
[34] J. M. Dreiling and T. J. Gay, *Chirally sensitive electron-induced molecular breakup and the Vester-Ulbricht hypothesis*, Phys. Rev. Lett. **113**, 118103 (2014).
[35] D. M. Campbell and P. S. Farago, *Spin-dependent electron scattering from optically active molecules*, Nature (London) **318**, 52 (1985).
[36] Stefan Mayer and Joachim Kessler, *Experimental verification of electron optic dichroism*, Phys. Rev. Lett. **74**, 4803 (1995).
[37] S. Mayer, C. Nolting, and J. Kessler, *Electron scattering from chiral molecules*, J. Phys. B **29**, 3497 (1996).
[38] A. Busalla, K. Blum, and D. G. Thompson, *Differential cross section for collisions between electrons and oriented chiral molecules*, Phys. Rev. Lett. **83**, 1562 (1999).

[39] M. Musigmann, A. Busalla, K. Blum, and D. G. Thompson, *Enantio-selective collisions between unpolarized electrons and chiral molecules*, J. Phys. B **34**, L79 (2001).

[40] D. Ray, B. Ulrich, I. Bocharova, C. Maharjan, P. Ranitovic, B. Gramkow, M. Magrakvelidze, S. De, I. V. Litvinyuk, A. T. Le, T. Morishita, C. D. Lin, G. G. Paulus, and C. L. Cocke, *Large-angle electron diffraction structure in laser-induced rescattering from rare gases*, Phys. Rev. Lett. **100**, 143002 (2008).

[41] M. Okunishi, T. Morishita, G. Prümper, K. Shimada, C. D. Lin, S. Watanabe, and K. Ueda, *Experimental retrieval of target structure information from laser-induced rescattered photoelectron momentum distributions*, Phys. Rev. Lett. **100**, 143001 (2008).

[42] M. Meckel, D. Comtois, D. Zeidler, A. Staudte, D. Pavičić, H. C. Bandulet, H. Pépin, J. C. Kieffer, R. Dörner, D. M. Villeneuve, and P. B. Corkum, *Laser-induced electron tunneling and diffraction*, Science **320**, 1478 (2008).

[43] Junliang Xu, Zhangjin Chen, Anh-Thu Le, and C. D. Lin, *Self-imaging of molecules from diffraction spectra by laser-induced rescattering electrons*, Phys. Rev. A **82**, 033403 (2010).

[44] Cosmin I. Blaga, Junliang Xu, Anthony D. DiChiara, Emily Sistrunk, Kaikai Zhang, Pierre Agostini, Terry A. Miller, Louis F. DiMauro, and C. D. Lin, *Imaging ultrafast molecular dynamics with laser-induced electron diffraction*, Nature (London) **483**, 194 (2012).

[45] Junliang Xu, Cosmin I. Blaga, Kaikai Zhang, Yu Hang Lai, C. D. Lin, Terry A. Miller, Pierre Agostini, and Louis F. DiMauro, *Diffraction using laser-driven broadband electron wave packets*, Nat. Commun. **5**, 4635 (2014).

[46] Michael G. Pullen, Benjamin Wolter, Anh-Thu Le, Matthias Baudisch, Michaël Hemmer, Arne Senftleben, Claus Dieter Schröter, Joachim Ullrich, Robert Moshammer, C. D. Lin, and Jens Biegert, *Imaging an aligned polyatomic molecule with laser-induced electron diffraction*, Nat. Commun. **6**, 7262 (2015).

[47] M. G. Pullen, B. Wolter, A.-T. Le, M. Baudisch, M. Sclafani, H. Pires, C. D. Schröter, J. Ullrich, R. Moshammer, T. Pfeifer, C. D. Lin, and J. Biegert, *Influence of orbital symmetry on diffraction imaging with rescattering electron wave packets*, Nat. Commun. **7**, 11922 (2016).

[48] Kasra Amini, Michele Sclafani, Tobias Steinle, Anh-Thu Le, Aurelien Sanchez, Carolin Müller, Johannes Steinmetzer, Lun Yue, José Ramón Martínez Saavedra, Michaël Hemmer *et al.*, *Imaging the Renner–Teller effect using laser-induced electron diffraction*, Proc. Natl. Acad. Sci. U.S.A. **116**, 8173 (2019).

[49] A. Sanchez, K. Amini, S.-J. Wang, T. Steinle, B. Belsa, J. Danek, A. T. Le, X. Liu, R. Moshammer, T. Pfeifer, M. Richter, J. Ullrich, S. Gräfe, C. D. Lin, and J. Biegert, *Molecular structure retrieval directly from laboratory-frame photoelectron spectra in laser-induced electron diffraction*, Nat. Commun. **12**, 1520 (2021).

[50] Kasra Amini and Jens Biegert, *Ultrafast electron diffraction imaging of gas-phase molecules*, in *Advances In Atomic, Molecular, and Optical Physics*, edited by Louis F. Dimauro, Hélène Perrin, and Susanne F. Yelin (Academic Press, New York, 2020), Vol. 69, Chap. 3, pp. 163–231.

[51] Umberto De Giovannini, Jochen Küpper, and Andrea Trabattoni, *New perspectives in time-resolved laser-induced electron diffraction*, J. Phys. B **56**, 054002 (2023).

[52] I. V. Litvinyuk, Kevin F. Lee, P. W. Dooley, D. M. Rayner, D. M. Villeneuve, and P. B. Corkum, *Alignment-dependent strong field ionization of molecules*, Phys. Rev. Lett. **90**, 233003 (2003).

[53] Domagoj Pavičić, Kevin F. Lee, D. M. Rayner, P. B. Corkum, and D. M. Villeneuve, *Direct measurement of the angular dependence of ionization for* N_2, O_2, *and* CO_2 *in intense laser fields*, Phys. Rev. Lett. **98**, 243001 (2007).

[54] B. Wolter, M. G. Pullen, A.-T. Le, M. Baudisch, K. Doblhoff-Dier, A. Senftleben, M. Hemmer, C. D. Schröter, J. Ullrich, T. Pfeifer, R. Moshammer, S. Gräfe, O. Vendrell, C. D. Lin, and J. Biegert, *Ultrafast electron diffraction imaging of bond breaking in di-ionized acetylene*, Science **354**, 308 (2016).

[55] M. Yu. Kuchiev, JETP Lett. Pis'ma Zh. Eksp. Teor. Fiz. **45**, 319 (1987), http://jetpletters.ru/ps/1241/article_18763.shtml.

[56] P. B. Corkum, *Plasma perspective on strong field multiphoton ionization*, Phys. Rev. Lett. **71**, 1994 (1993).

[57] K. J. Schafer, Baorui Yang, L. F. DiMauro, and K. C. Kulander, *Above threshold ionization beyond the high harmonic cutoff*, Phys. Rev. Lett. **70**, 1599 (1993).

[58] M. Lewenstein, Ph. Balcou, M. Yu. Ivanov, Anne L'Huillier, and P. B. Corkum, *Theory of high-harmonic generation by low-frequency laser fields*, Phys. Rev. A **49**, 2117 (1994).

[59] P. Salières, B. Carré, L. Le Déroff, F. Grasbon, G. G. Paulus, H. Walther, R. Kopold, W. Becker, D. B. Milošević, A. Sanpera *et al.*, *Feynman's path-integral approach for intense-laser-atom interactions*, Science **292**, 902 (2001).

[60] P. Agostini, F. Fabre, G. Mainfray, G. Petite, and N. K. Rahman, *Free-free transitions following six-photon ionization of xenon atoms*, Phys. Rev. Lett. **42**, 1127 (1979).

[61] A. McPherson, G. Gibson, H. Jara, U. Johann, T. S. Luk, I. McIntyre, K. Boyer, and C. K. Rhodes, *Studies of multiphoton production of vacuum-ultraviolet radiation in the rare gases*, J. Opt. Soc. Am. B **4**, 595 (1987).

[62] M. Ferray, A. L'Huillier, X. F. Li, L. A. Lompre, G. Mainfray, and C. Manus, *Multiple-harmonic conversion of 1064 nm radiation in rare gases*, J. Phys. B **21**, L31 (1988).

[63] G. G. Paulus, W. Nicklich, Huale Xu, P. Lambropoulos, and H. Walther, *Plateau in above threshold ionization spectra*, Phys. Rev. Lett. **72**, 2851 (1994).

[64] J. Itatani, J. Levesque, D. Zeidler, H. Niikura, H. Pepin, J. C. Kieffer, P. B. Corkum, and D. M. Villeneuve, *Tomographic imaging of molecular orbitals*, Nature (London) **432**, 867 (2004).

[65] J. P. Marangos, *Development of high harmonic generation spectroscopy of organic molecules and biomolecules*, J. Phys. B **49**, 132001 (2016).

[66] Peng Peng, Claude Marceau, and David M. Villeneuve, *Attosecond imaging of molecules using high harmonic spectroscopy*, Nat. Rev. Phys. **1**, 144 (2019).

[67] Michael Spanner, Olga Smirnova, Paul B. Corkum, and Misha Yu Ivanov, *Reading diffraction images in strong field ionization of diatomic molecules*, J. Phys. B **37**, L243 (2004).

[68] D. Shafir, B. Fabre, J. Higuet, H. Soifer, M. Dagan, D. Descamps, E. Mével, S. Petit, H. J. Wörner, B. Pons, N. Dudovich, and Y. Mairesse, *Role of the ionic potential in high harmonic generation*, Phys. Rev. Lett. **108**, 203001 (2012).

[69] R. Kopold, D. B. Milošević, and W. Becker, *Rescattering processes for elliptical polarization: A quantum trajectory analysis*, Phys. Rev. Lett. **84**, 3831 (2000).

[70] XuanYang Lai, ChuanLiang Wang, YongJu Chen, ZiLong Hu, Wei Quan, XiaoJun Liu, Jing Chen, Ya Cheng, ZhiZhan Xu, and Wilhelm Becker, *Elliptical polarization favors long quantum orbits in high-order above-threshold ionization of noble gases*, Phys. Rev. Lett. **110**, 043002 (2013).

[71] Misha Yu Ivanov, Michael Spanner, and Olga Smirnova, *Anatomy of strong field ionization*, J. Mod. Opt. **52**, 165 (2005).

[72] Jizhou Yu, Xufei Sun, Yun Shao, Min Li, Qihuang Gong, and Yunquan Liu, *Retrieving the ionization dynamics of high-energy photoelectrons in elliptically polarized laser fields*, Phys. Rev. A **92**, 043411 (2015).

[73] A. S. Alnaser, X. M. Tong, T. Osipov, S. Voss, C. M. Maharjan, P. Ranitovic, B. Ulrich, B. Shan, Z. Chang, C. D. Lin, and C. L. Cocke, *Routes to control of* H_2 *Coulomb explosion in few-cycle laser pulses*, Phys. Rev. Lett. **93**, 183202 (2004).

[74] Andrea Trabattoni, Joss Wiese, Umberto De Giovannini, Jean-François Olivieri, Terry Mullins, Jolijn Onvlee, Sang-Kil Son, Biagio Frusteri, Angel Rubio, Sebastian Trippel, and Jochen Küpper, *Setting the photoelectron clock through molecular alignment*, Nat. Commun. **11**, 2546 (2020).

[75] XiaoLei Hao, YuXing Bai, XiaoYun Zhao, Chan Li, JingYu Zhang, JiLing Wang, WeiDong Li, ChuanLiang Wang, Wei Quan, XiaoJun Liu, Zheng Shu, Mingqing Liu, and Jing Chen, *Effect of Coulomb field on laser-induced ultrafast imaging methods*, Phys. Rev. A **101**, 051401(R) (2020).

[76] D. G. Thompson, *Chiral effects in the scattering of electrons by molecules*, Can. J. Phys. **74**, 920 (1996).

[77] H. Stapelfeldt and T. Seideman, *Colloquium: Aligning molecules with strong laser pulses*, Rev. Mod. Phys. **75**, 543 (2003).

[78] Lotte Holmegaard, Jonas L. Hansen, Line Kalhøj, Sofie Louise Kragh, Henrik Stapelfeldt, Frank Filsinger, Jochen Küpper, Gerard Meijer, Darko Dimitrovski, Mahmoud Abu-samha, Christian P. J. Martiny, and Lars Bojer Madsen, *Photoelectron angular distributions from strong-field ionization of oriented molecules*, Nat. Phys. **6**, 428 (2010).

[79] Adam S. Chatterley, Constant Schouder, Lars Christiansen, Benjamin Shepperson, Mette Heidemann Rasmussen, and Henrik Stapelfeldt, *Long-lasting field-free alignment of large molecules inside helium nanodroplets*, Nat. Commun. **10**, 133 (2019).

[80] Jochen Mikosch, Andrey E. Boguslavskiy, Iain Wilkinson, Michael Spanner, Serguei Patchkovskii, and Albert Stolow, *Channel- and angle-resolved above threshold ionization in the molecular frame*, Phys. Rev. Lett. **110**, 023004 (2013).

[81] Felix Schell, Timm Bredtmann, Claus Peter Schulz, Serguei Patchkovskii, Marc J. J. Vrakking, and Jochen Mikosch, *Molecular orbital imprint in laser-driven electron recollision*, Sci. Adv. **4**, eaap8148 (2018).

[82] Jochen Maurer, Darko Dimitrovski, Lauge Christensen, Lars Bojer Madsen, and Henrik Stapelfeldt, *Molecular-frame 3D photoelectron momentum distributions by tomographic reconstruction*, Phys. Rev. Lett. **109**, 123001 (2012).

[83] Joss Wiese, Jolijn Onvlee, Sebastian Trippel, and Jochen Küpper, *Strong-field ionization of complex molecules*, Phys. Rev. Res. **3**, 013089 (2021).

[84] X. M. Tong, Z. X. Zhao, and C. D. Lin, *Theory of molecular tunneling ionization*, Phys. Rev. A **66**, 033402 (2002).

[85] Thomas K. Kjeldsen, Christer Z. Bisgaard, Lars Bojer Madsen, and Henrik Stapelfeldt, *Influence of molecular symmetry on strong-field ionization: Studies on ethylene, benzene, fluorobenzene, and chlorofluorobenzene*, Phys. Rev. A **71**, 013418 (2005).

[86] P. Dietrich and P. B. Corkum, *Ionization and dissociation of diatomic molecules in intense infrared laser fields*, J. Chem. Phys. **97**, 3187 (1992).

[87] Jérôme Levesque, Yann Mairesse, Nirit Dudovich, Henri Pépin, Jean-Claude Kieffer, P. Corkum, and D. Villeneuve, *Polarization state of high-order harmonic emission from aligned molecules*, Phys. Rev. Lett. **99**, 243001 (2007).

[88] D. Shafir, Y. Mairesse, D. M. Villeneuve, P. B. Corkum, and N. Dudovich, *Atomic wavefunctions probed through strong-field light–matter interaction*, Nat. Phys. **5**, 412 (2009).

[89] R. Cireasa, A. E. Boguslavskiy, B. Pons, M. C. H. Wong, D. Descamps, S. Petit, H. Ruf, N. Thiré, A. Ferré, J. Suarez, J. Higuet, B. E. Schmidt, A. F. Alharbi, F. Légaré, V. Blanchet, B. Fabre, S. Patchkovskii, O. Smirnova, Y. Mairesse, and V. R. Bhardwaj, *Probing molecular chirality on a sub-femtosecond timescale*, Nat. Phys. **11**, 654 (2015).

[90] Ivan Powis, *Photoelectron circular dichroism of the randomly oriented chiral molecules glyceraldehyde and lactic acid*, J. Chem. Phys. **112**, 301 (2000).

[91] C. Stefan Lehmann, N. Bhargava Ram, Ivan Powis, and Maurice H. M. Janssen, *Imaging photoelectron circular dichroism of chiral molecules by femtosecond multiphoton coincidence detection*, J. Chem. Phys. **139**, 234307 (2013).

[92] E. Bloch, S. Larroque, S. Rozen, S. Beaulieu, A. Comby, S. Beauvarlet, D. Descamps, B. Fabre, S. Petit, R. Taïeb, A. J. Uzan, V. Blanchet, N. Dudovich, B. Pons, and Y. Mairesse, *Revealing the influence of molecular chirality on tunnel-ionization dynamics*, Phys. Rev. X **11**, 041056 (2021).

[93] M. Wollenhaupt, M. Krug, J. Köhler, T. Bayer, C. Sarpe-Tudoran, and T. Baumert, *Three-dimensional tomographic reconstruction of ultrashort free electron wave packets*, Appl. Phys. B **95**, 647 (2009).

[94] W. Becker, S. P. Goreslavski, D. B. Milošević, and G. G. Paulus, *The plateau in above-threshold ionization: The keystone of rescattering physics*, J. Phys. B **51**, 162002 (2018).

[95] Wilhelm Becker and Dejan B. Milošević, *Elliptic dichroism in strong-field ionization of atoms subjected to tailored laser fields*, Phys. Chem. Chem. Phys. **24**, 7014 (2022).

[96] C. Figueira de Morisson Faria and A. S. Maxwell, *It is all about phases: Ultrafast holographic photoelectron imaging*, Rep. Prog. Phys. **83**, 034401 (2020).

[97] N. Dudovich, J. Levesque, O. Smirnova, D. Zeidler, D. Comtois, M. Ivanov, D. Villeneuve, and P. Corkum, *Attosecond temporal gating with elliptically polarized light*, Phys. Rev. Lett. **97**, 253903 (2006).

[98] K. S. Budil, P. Salières, M. D. Perry, and Anne L'Huillier, *Influence of ellipticity on harmonic generation*, Phys. Rev. A **48**, R3437 (1993).

[99] Maurice Tia, Martin Pitzer, Gregor Kastirke, Janine Gatzke, Hong-Keun Kim, Florian Trinter, Jonas Rist, Alexander Hartung, Daniel Trabert, Juliane Siebert *et al.*, *Observation of enhanced chiral asymmetries in the inner-shell photoionization of uniaxially oriented methyloxirane enantiomers*, J. Phys. Chem. Lett. **8**, 2780 (2017).

[100] K. Fehre, S. Eckart, M. Kunitski, C. Janke, D. Trabert, M. Hofmann, J. Rist, M. Weller, A. Hartung, L. Ph. H. Schmidt, T. Jahnke, H. Braun, T. Baumert, J. Stohner, Ph. V. Demekhin, M. S. Schöffler, and R. Dörner, *Strong differential photoion circular dichroism in strong-field ionization of chiral molecules*, Phys. Rev. Lett. **126**, 083201 (2021).

[101] Václav Hanus, Sarayoo Kangaparambil, Martin Richter, Lukas Haßfurth, Martin Dorner-Kirchner, Gerhard G. Paulus, Xinhua Xie, Andrius Baltuška, Stefanie Gräfe, and Markus Zeiler, *Carrier envelope phase sensitivity of photoelectron circular dichroism*, Phys. Chem. Chem. Phys. **25**, 4656 (2023).

[102] Misha Yu, Ivanov, Thomas Brabec, and Neal Burnett, *Coulomb corrections and polarization effects in high-intensity high-harmonic emission*, Phys. Rev. A **54**, 742 (1996).

[103] Michael Spanner, *Field-free alignment and strong field control of molecular rotors*, Ph.D. thesis, University of Waterloo, 2004.

[104] Donatella Loru, Miguel A. Bermúdez, and M. Eugenia Sanz, *Structure of fenchone by broadband rotational spectroscopy*, J. Chem. Phys. **145**, 074311 (2016).

[105] Lothar Schäfer, *Electron diffracion as a tool of structural chemistry*, Appl. Spectrosc. **30**, 123 (1976).

[106] P. G. Burke, *R-Matrix Theory of Atomic Collisions: Application to Atomic, Molecular and Optical Processes*, Springer Series on Atomic, Optical, and Plasma Physics (Springer, Berlin, 2011).

[107] D. C. Griffin and M. S. Pindzola, *Differential excitation cross sections for electron impact on* Li^+*: A study of continuum coupling effects*, Phys. Rev. A **42**, 248 (1990).

[108] Jonathan Tennyson, *Electron–molecule collision calculations using the R-matrix method*, Phys. Rep. **491**, 29 (2010).

[109] Zdeněk Mašín, Jakub Benda, Jimena D. Gorfinkiel, Alex G. Harvey, and Jonathan Tennyson, *UKRmol+: A suite for modelling electronic processes in molecules interacting with electrons, positrons and photons using the R-matrix method*, Comput. Phys. Commun. **249**, 107092 (2020).

[110] M. E. Rose, *Elementary Theory of Angular Momentum*, Structure of Matter Series (Wiley, New York, 1957).

[111] B. H. Bransden and C. J. Joachain, *Physics of Atoms and Molecules* (Pearson Education, Harlow, England, 2003).

[112] N. M Kabachnik, *Screening and antiscreening in the semiclassical description of ionization in fast ion-atom collisions*, J. Phys. B **26**, 3803 (1993).

[113] T. Kirchner, M. Horbatsch, H. J. Lüdde, and R. M. Dreizler, *Time-dependent screening effects in ion-atom collisions with many active electrons*, Phys. Rev. A **62**, 042704 (2000).

[114] Lucilla Alagna, Tommaso Prosperi, Stefano Turchini, José Goulon, Andrei Rogalev, Chantal Goulon-Ginet, Calogero R. Natoli, Robert D. Peacock, and Brian Stewart, *X-ray natural circular dichroism*, Phys. Rev. Lett. **80**, 4799 (1998).

[115] Robert D. Peacock and Brian Stewart, *Natural circular dichroism in x-ray spectroscopy*, J. Phys. Chem. B **105**, 351 (2001).

[116] Yu Zhang, Jérémy R. Rouxel, Jochen Autschbach, Niranjan Govind, and Shaul Mukamel, *X-ray circular dichroism signals: A unique probe of local molecular chirality*, Chem. Sci. **8**, 5969 (2017).

[117] P. Colosimo, G. Doumy, C. I. Blaga, J. Wheeler, C. Hauri, F. Catoire, J. Tate, R. Chirla, A. M. March, G. G. Paulus, H. G. Muller, P. Agostini, and L. F. DiMauro, *Scaling strong-field interactions towards the classical limit*, Nat. Phys. **4**, 386 (2008).

[118] C. Cornaggia, *Molecular potential anisotropy probed by electron rescattering in strong-field ionization of molecules*, Phys. Rev. A **103**, 013102 (2021).

[119] Kilian Fehre, Sebastian Eckart, Maksim Kunitski, Christian Janke, Daniel Trabert, Jonas Rist, Miriam Weller, Alexander Hartung, Lothar Ph. H. Schmidt, Till Jahnke, Reinhard Dörner, and Markus Schöffler, *Link between photoelectron circular dichroism and fragmentation channel in strong field ionization*, J. Phys. Chem. A **123**, 6491 (2019).

[120] Ingo Barth and Olga Smirnova, *Spin-polarized electrons produced by strong-field ionization*, Phys. Rev. A **88**, 013401 (2013).

[121] Alexander Hartung, Felipe Morales, Maksim Kunitski, Kevin Henrichs, Alina Laucke, Martin Richter, Till Jahnke, Anton Kalinin, Markus Schöffler, Lothar Ph H. Schmidt, Misha Ivanov, Olga Smirnova, and Reinhard Dörner, *Electron spin polarization in strong-field ionization of xenon atoms*, Nat. Photonics **10**, 526 (2016).

[122] K. Ray, S. P. Ananthavel, D. H. Waldeck, and R. Naaman, *Asymmetric scattering of polarized electrons by organized organic films of chiral molecules*, Science **283**, 814 (1999).

[123] Ron Naaman and David H. Waldeck, *Spintronics and chirality: Spin selectivity in electron transport through chiral molecules*, Annu. Rev. Phys. Chem. **66**, 263 (2015).

[124] Karen Michaeli, Nirit Kantor-Uriel, Ron Naaman, and David H. Waldeck, *The electron's spin and molecular*

chirality—How are they related and how do they affect life processes?, Chem. Soc. Rev. **45**, 6478 (2016).

[125] Chidambar Kulkarni, Amit Kumar Mondal, Tapan Kumar Das, Gal Grinbom, Francesco Tassinari, Mathijs F. J. Mabesoone, E. W. Meijer, and Ron Naaman, *Highly efficient and tunable filtering of electrons' spin by supramolecular chirality of nanofiber-based materials*, Adv. Mater. **32**, 1904965 (2020).

[126] N. Fedorov, S. Beaulieu, A. Belsky, V. Blanchet, R. Bouillaud, M. De Anda Villa, A. Filippov, C. Fourment, J. Gaudin, R. E. Grisenti *et al.*, *Aurore: A platform for ultrafast sciences*, Rev. Sci. Instrum. **91**, 105104 (2020).

[127] Pascal Salières, Anne L'Huillier, and Maciej Lewenstein, *Coherence control of high-order harmonics*, Phys. Rev. Lett. **74**, 3776 (1995).

[128] M. Bellini, C. Lyngå, A. Tozzi, M. B. Gaarde, T. W. Hänsch, A. L'Huillier, and C. G. Wahlström, *Temporal coherence of ultrashort high-order harmonic pulses*, Phys. Rev. Lett. **81**, 297 (1998).

[129] J. Higuet, H. Ruf, N. Thiré, R. Cireasa, E. Constant, E. Cormier, D. Descamps, E. Mével, S. Petit, B. Pons, Y. Mairesse, and B. Fabre, *High-order harmonic spectroscopy of the Cooper minimum in argon: Experimental and theoretical study*, Phys. Rev. A **83**, 053401 (2011).

[130] F. Cloux, B. Fabre, and B. Pons, *Semiclassical description of high-order-harmonic spectroscopy of the Cooper minimum in krypton*, Phys. Rev. A **91**, 023415 (2015).

[131] D. J. W. Hardie and R. E. Olson, *Charge transfer and ionisation processes involving multiply charged ions in collision with atomic hydrogen*, J. Phys. B **16**, 1983 (1983).

[132] L. F. Errea, Clara Illescas, L. Méndez, B. Pons, A. Riera, and J. Suárez, *Accuracy of the classical trajectory Monte Carlo method for electron capture in* Li^{3+} *and* $Ne^{10+} + H(1s)$ *collisions*, Phys. Rev. A **70**, 052713 (2004).

[133] P. Botheron and B. Pons, *One-electron atom in a strong and short laser pulse: Comparison of classical and quantum descriptions*, Phys. Rev. A **80**, 023402 (2009).

[134] S. A. Kelvich, W. Becker, and S. P. Goreslavski, *Coulomb focusing and defocusing in above-threshold-ionization spectra produced by strong mid-IR laser pulses*, Phys. Rev. A **93**, 033411 (2016).

[135] Laibing Wang, Lu Yin, Wei Zhang, Xiulin Zhu, and Michiya Fujiki, *Circularly polarized light with sense and wavelengths to regulate azobenzene supramolecular chirality in optofluidic medium*, J. Am. Chem. Soc. **139**, 13218 (2017).

[136] H. Soifer, P. Botheron, D. Shafir, A. Diner, O. Raz, B. Bruner, Y. Mairesse, B. Pons, and N. Dudovich, *Near-threshold high-order harmonic spectroscopy with aligned molecules*, Phys. Rev. Lett. **105**, 143904 (2010).

[137] Dror Shafir, Hadas Soifer, Barry D. Bruner, Michal Dagan, Yann Mairesse, Serguei Patchkovskii, Misha Yu Ivanov, Olga Smirnova, and Nirit Dudovich, *Resolving the time when an electron exits a tunnelling barrier*, Nature (London) **485**, 343 (2012).

[138] Milton Abramowitz and Irene A. Stegun, *Handbook of Mathematical Functions with Formulas, Graphs, and Mathematical Tables* (Dover, New York, 1964).

[139] Dan Dill and J. L. Dehmer, *Electron-molecule scattering and molecular photoionization using the multiple-scattering method*, J. Chem. Phys. **61**, 692 (1974).

[140] P. Hohenberg and W. Kohn, *Inhomogeneous electron gas*, Phys. Rev. **136**, B864 (1964).

[141] Axel D. Becke, *Density-functional thermochemistry. III. The role of exact exchange*, J. Chem. Phys. **98**, 5648 (1993).

[142] P. J. Stephens, F. J. Devlin, C. F. Chabalowski, and M. J. Frisch, *Ab initio calculation of vibrational absorption and circular dichroism spectra using density functional force fields*, J. Phys. Chem. **98**, 11623 (1994).

[143] R. Krishnan, J. S. Binkley, R. Seeger, and J. A. Pople, *Self-consistent molecular orbital methods. XX. A basis set for correlated wave functions*, J. Chem. Phys. **72**, 650 (1980).

[144] Timothy Clark, Jayaraman Chandrasekhar, Günther W. Spitznagel, and Paul Von Ragué Schleyer, *Efficient diffuse function-augmented basis sets for anion calculations. III. The* 3–21 + G *basis set for first-row elements, Li–F*, J. Comput. Chem. **4**, 294 (1983).

[145] Thom H. Dunning, *Gaussian basis functions for use in molecular calculations. I. Contraction of* $(9s5p)$ *atomic basis sets for the first-row atoms*, J. Chem. Phys. **53**, 2823 (1970).

[146] Thom. H. Dunning and P. Jeffrey Hay, *Gaussian basis sets for molecular calculations*, in *Methods of Electronic Structure Theory*, edited by Henry F. Schaefer (Springer US, Boston, 1977), pp. 1–27.